ALMA MATER STUDIORUM · UNIVERSITY OF BOLOGNA

School of Science
Department of Physics and Astronomy
Master's Degree in Physics

UPSCALING OF A MONOLITHIC, PHOTOVOLTAIC – ASSISTED WATER PHOTOELECTROLYSIS DEVICE IN ALKALINE MEDIA

Supervisor:
Prof. Luca Pasquini

Co-supervisor:
Prof. Sabrina Sartori

Submitted by:
Antonio Barile

Academic Year 2022/2023

Acknowledgements

This thesis is written for a Master's degree in Physics, curriculum "Materials Physics and Nanoscience" at the Department of Physics, University of Bologna. The journey leading to this work took place between March 2023 and September 2023 in Oslo, Norway, as part of an international thesis project supported by the "Innovation grants" program at the University of Oslo (UiO), under the project titled "Towards upscaling sustainable green hydrogen production" (project number 102419118).
First and foremost, I would like to express my gratitude to my dedicated supervisors, Luca Pasquini, and Sabrina Sartori, for giving me this opportunity to widen my experience and knowledge in this field. Your advice and constant encouragement have been very helpful for me in conducting this work, along with the chance to be in projects carried out at the Department of Technology Systems (ITS) at Kjeller. Thanks to everyone in the group of Electrochemistry at Forksningsparken, Oslo, and to the ITS group for all the social activities, for providing everything that I need for this thesis, and for spreading a great friendly environment. Their collaborative spirit and the resources they offered played a pivotal role during my experience.
A special appreciation goes to Marco Blasius from the Helmholtz Institute Erlangen-Nuremberg for Renewable Energy (HI-ERN) for his incredible help with the setup assembling and its crucial support to identify all the pitfalls in its scaling up. Thanks to Junjie Zhu from IFE who assembled the PV-EC device. Thanks also to Henrik Petlund for his work in the OER catalysts.
Lastly, I would like to thank my experimental supervisor Athanasios Chatzitakis, for his help in completing the PV-EC device, and for giving me insights and ideas on how to build the whole system. I am deeply thankful for his presence as a supportive mentor throughout this endeavor.

Abstract

The goal of this thesis is to experimentally study the performance and the characteristics of an up-scaled Photovoltaic-assisted electrochemical cell. Specifically, an amorphous silicon PV was sandwiched between an anode, with a double perovskite cobaltite as a catalyst, and an electrodeposited Ni-Mo on a titanium foil cathode.
Firstly, the device's design was prepared and then built in the laboratory. Then, the whole chassis was assembled, with the anion exchange membranes, the O-rings, and the PV-E cell, along with the stainless steel skeleton where eight screws were placed to pressurize the device and better isolate it from the alkaline solution (KOH) where it was placed in. The bigger box was then connected to a reservoir to recycle the electrolyte and to collect both hydrogen and oxygen through a peristaltic pump.
Successively, the illuminated response was estimated through a solar simulator, with the water displacement method as a tool to evaluate the volumetric production rate of H_2 gas. Unfortunately, the low rate of the produced gasses and the overall complexity of the setup hindered the possibility of collecting quantitative data. Nevertheless, the PV-E cell is completely functioning, and the formation of bubbles that can be seen in the quartz window of the device, due to the water-splitting process occurring at the electrode's surface, proves the correct operation of the up-scaled cell.
However, from a future work perspective, several adjustments are needed to consider this project as a functioning reactor. Both engineering and chemical issues need to be solved to allow the measurement of the produced gases.

Contents

List of Figures

List of Abbreviations

TW	TeraWatt
AM1.5G	Air Mass 1.5 atmosphere thickness Global - Global Standard Spectrum
Ag	Silver Element
HBE	Hydrogen Binding Energy
NP	Nanoparticle
CO_2	Carbon Dioxide
H_2O	Water Molecule
H_2	Hydrogen Molecule
O_2	Oxygen Molecule
PEC	PhotoElectrochemical
PV	Photovoltaic
PV-E	Photovoltaic - Electrolysis
Ir	Iridium Element
Ru	Ruthenium Element
PEM	Polymer Electrolyte Membrane
ea	earth-abundant
OER	Oxygen Evolution Reaction
HER	Hydrogen Evolution Reaction
AEMs	Anion Exchange Membranes
PEMs	Proton Exchange Membranes
BPMs	Bipolar Membranes
NHE	Normal Hydrogen Electrode
RHE	Reversible Hydrogen Electrode
M	Mole
OH	Hydroxide
PZC	Point of Zero Charge
ihp	Inner Helmholtz Plane
ohp	Outer Helmholtz Plane
SCR	Space Charge Region
STH	Solar-To-Hydrogen
IPCE	Incident Photon-to-current Conversion Efficiency
APCE	Absorbed Photon-to-current Conversion Efficiency
EQE	External Quantum Efficiency
$SrTiO_3$	Strontium Titanate
Ti	Titanium Element

Si	Silicon Element
$a-Si$	amorphous Silicon
TCO	Transparent Conductive Oxide
DFT	Density Functional Theory
KOH	Potassium Hydroxide
FTO	Fluorine-doped Tin Oxide
Pt	Platinum Element
$BiVO_4$	Bismuth Vanadate
EC	ElectroChemical
Co	Cobalt Element
REF	Reference Electrode
CE	Counter Electrode
WE	Working Electrode
BGLC	$Ba_{1-x}Gd_{1-y}La_{x+y}Co_2O_{6-\delta}$
$NiMo$	Nickel Molybdenum Alloy
SnO_2	Tin(IV) Oxide - Stannic Oxide
PERC	Passivated Emitter and Rear Cell
PVC	Polyvinyl chloride
PE	Polyethylene
EVA	Ethylene Vinyl Acetate
PLD	Pulsed Laser Deposition
ARC	Anti Reflection Coating
F	Faraday Constant
Ba	Barium Element
Gd	Gadolinium Element
La	Lanthanum Element
LOM	Lattice Oxygen Oxidation Mechanism
AEM	Adsorbate Evolution Mechanism
NH_3	Ammonia
IrO_2	Iridium Oxide
RuO_2	Ruthenium Oxide
RuO_4	Ruthenium Tetroxide
BGLC587	$Ba_{0.5}Gd_{0.8}La_{0.7}Co_2O_{6-\delta}$
BSCF82	$Ba_{0.5}Sr_{0.5}Co_{0.8}Fe_{0.2}O_{3-\delta}$
BGLCF70	$Ba_{0.5}Gd_{0.8}La_{0.7}Co_{0.6}Fe_{1.4}O_{6-\delta}$

Chapter 1

Introduction

1.1 Summary

The energy problem stands as one of the primary challenges confronting humanity today. In the twenty-first century, the pursuit of an adequate energy supply to meet the demands of the global population remains a driving force. As of 2021, the world's energy consumption rate stands at 17.6 TW, with oil, coal, and natural gas accounting for approximately 81% of the energy supply [1]. However, projections indicate a significant surge to 27.6 TW by 2050, highlighting the inability of fossil fuels to keep pace with escalating global demand [2].
More importantly, the environmental consequences of such energy sources are no longer acceptable nowadays, due to the impending climate collapse. The main concern is the alarming rise in atmospheric CO_2 levels, which poses a severe threat of global warming exceeding 2°C. Such a temperature increase could have catastrophic impacts on ecosystems and human society at large. Therefore, the imperative to reduce our reliance on fossil fuels and embrace renewable energy sources has become paramount. Sustainable energy sources include wind, hydroelectric, nuclear, and solar. The latter is the most promising one, with significant and fast growth in the solar cell market.
However, due to its intermittent nature, solar electricity alone cannot serve as the primary energy source. Consequently, the need for energy storage arises, which can be achieved through three methods: batteries, mechanical or gravity systems, and chemical fuels. Among these options, chemical fuels offer advantages such as high energy storage densities and ease of transportation, although their efficiency may be relatively low. This is particularly evident in the case of artificial photosynthesis, which combines these benefits but suffers from inefficiency.
Typical chemical fuels include methane, diesel, gasoline, hydrogen, etc. Ideally, capturing the CO_2 emissions from fossil fuels and reusing them to synthesize chemical fuels would be the preferred route. However, the direct photo-electrochemical conversion of CO_2 into fuel presents significant challenges, mainly due to the intricate electron transfer steps involved in the electrochemical half-reactions.

Therefore, the most viable pathway for converting solar energy into a usable fuel appears to be through the production of hydrogen. An example of this is water splitting, which involves the evolution of oxygen as one component and the generation of a reduced fuel (hydrogen) as the other. Its reaction can be written as follows:

$$2H_2O + \text{sunlight} \rightleftharpoons 2H_2 + O_2 \quad \Delta G = 237 kJ/mol.$$

The reduction half-reaction is a simple two-electron transfer reaction, while four electrons are involved in the oxidation of water to form oxygen. However, energy is required to cleave H−O−H bonds. Many pathways exist for the conversion of water and sunlight into hydrogen. The one that will be discussed in this thesis will be photoelectrochemical (PEC) water splitting. Its main advantages are the possibility to produce hydrogen and oxygen at separated electrodes, can be carried at room temperature, and that the device can be built entirely from inorganic materials.

1.2 Motivation

The PEC device provides several advantages. Firstly, it enables the easy separation of gases, eliminating safety concerns associated with the hazardous mixture of hydrogen and oxygen. The explosive limits for this mixture range from 18% to 59%, while the flammability limits span from 4% to 74% in the air. Secondly, it circumvents the need for large-scale solar concentrators, which would otherwise restrict its application to sunny regions and large central facilities. This widens the potential usage of these devices. Lastly, PEC devices offer a higher degree of chemical robustness and durability compared to organic or biological systems, making them more reliable in practical applications.
Furthermore, the PEC approach offers two potential advantages concerning photovoltaic (PV) - electrolysis systems. The first lies in the fact that commercial electrolyzers typically require cell voltages of $\sim 1.9\ V$ to achieve optimal operating current densities of $\sim 1\ A/cm^2$. Since the thermodynamically required potential for water splitting is 1.23 V, this places an upper limit of 65% (1.23 / 1.9) on the overall energy conversion efficiency in conventional systems [3]. In contrast, the current density at a semiconductor photoelectrode immersed in water is much smaller ($10 - 20\ mA/cm^2$ at most) and the required overpotential is therefore substantially lower, depending on the catalytic activity of the semiconductor surface.
The second advantage is that a PEC system can be constructed as a single, monolithic device. This requires fewer packaging components (frame, glass, connections, etc.) and may lead to significantly lower costs.
Immense efforts have been devoted to the electrolysis and photoelectrolysis of water, and the main challenges focus on the complex four-electron oxygen evolution reaction (OER) and the stability of the (photoelectro-)catalysts. Additionally, the lack of highly efficient catalyst elements, such as Iridium (Ir) and Ruthenium (Ru), jeopardizes this goal. The amounts of Ir and Ru that are needed to achieve 1 TW of hydrogen through the state-of-the-art polymer electrolyte

membrane (PEM) electrolyzer represent 180 and 12 years of the current annual productions of Ir and Ru, respectively [4].
Therefore, the development of efficient and robust catalysts based on earth-abundant (ea) elements is crucial to increasing the share of water electrolysis in global hydrogen production. In that direction, oxide perovskites ABO_3 have shown high efficiency and stability for the OER in alkaline water electrolysis.

1.3 Research Questions

In this thesis, a scale-up of a previous work [5] is investigated, in particular, a family of double perovskite cobaltites is considered as catalysts for the OER in alkaline media at room temperature in a 10 cm^2 PEC device. Its design is inspired by a study with some modifications [6]. The use of three Anion Exchange Membranes (AEMs) is needed to safely separate hydrogen and oxygen, and a system of pumping allows the circulation of the electrolyte and the collection of the production gasses.
The research questions that drive this project are the following:

- By scaling up a smaller PV-PEC device, what will be the performance difference?
- What will be the modifications in both the activity and stability of the device?
- It is possible to just increase the size of a cell, even if it is made of promising catalyst materials, to surpass the "laboratory" step and reach the "industrial" one? Or some extra precautions are needed? Is the trade-off worth the effort?

1.4 Structure of the Thesis

This thesis will be divided into two theoretical chapters, one experimental section, and a discussion part with the results. In the first chapter, photoelectrocatalysis will be discussed, with several subsections on the solar cell structure, the electrode/electrolyte interface, along with the HER and OER processes, and the PV-PEC cell under operating conditions. The photocurrent, the efficiency, and the hydrogen production rate are defined, highlighting the importance of these parameters in the performance of a PV-PEC device.
The second chapter will deal with the state of the art of real devices: single-junction will be discussed with both limits and losses. Later on, multi-junctions will be investigated, their design and their optical properties. A major focus will be held on the monolithic PV-E tandem configuration and the upcoming challenges that need to be overcome, like up-scaling and membrane-related ones.
Then, an experimental chapter will show the instrumentation, the materials characterization, and the chosen design for the final device, along with its creative process. The acquisition data

section will consider the measurement procedure with the solar simulator and the leakage tests. Finally, the data will be interpreted in the results chapter, along with the answers to the research questions, which will be further analyzed together with the consideration of future work in the conclusions section.

Chapter 2

Basic Principles of Photoelectrocatalysis

Photoelectrochemical water splitting is categorized among the six most promising pathways for producing renewable hydrogen gas [7]. It has roots back in 1972 with the pioneering work of Fujishima and Honda that spawned the modern field of artificial photosynthesis [8]. Here, the electrolysis of water is promoted by one or more semiconductor photoelectrodes, able to harvest the incoming photons and direct the photogenerated charges towards the splitting of H_2O into H_2. The hydrogen and oxygen gases are produced at distinct electrodes, enabling convenient separation. This stands in contrast to the conventional photocatalytic approach, where the lack of physical separation in a homogeneous environment makes gas separation more challenging.

2.1 The Photoelectrochemical Cell

The simplified energy diagram of a photoelectrochemical (PEC) cell, depicted in Fig. 2.1, illustrates its key components: a single photoanode and a metal counter electrode. The main component of the PEC cell is the semiconductor, which converts incident photons to electron–hole pairs. The photogenerated electrons, separated from the holes by an electric field, migrate toward the conducting back contact and are transported to the metal counter-electrode via an external wire. At the metal, the electrons participate in the reduction of water, ultimately forming hydrogen gas. On the other hand, the photogenerated holes are swept toward the semiconductor/electrolyte interface, where they engage in the oxidation of water, leading to the generation of oxygen gas.
So two half-reactions are involved and they must happen simultaneously: the oxygen evolution reaction (OER) and the hydrogen evolution reaction (HER). Considering the case of an alkaline electrolyte, the reduction and the oxidation reactions can be represented as follows:

$$OER : 4\,OH^- + 4\,h^+ \rightleftharpoons 2H_2O + O_2 \quad E^0_{ox} = -0.401\ V\ vs.\ NHE$$
$$HER : 4\,H_2O + 4\,e^- \rightleftharpoons 2\,H_2 + 4\,OH^- \quad E^0_{red} = -0.828\ V\ vs.\ NHE$$

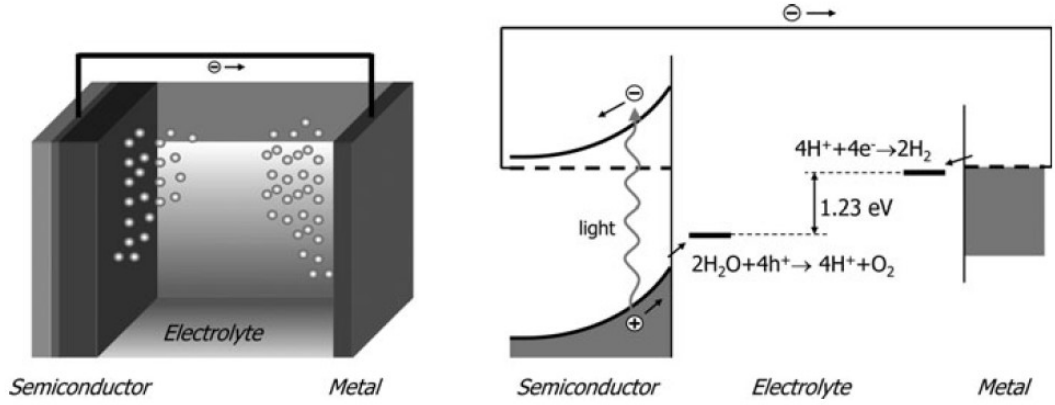

Figure 2.1: Illustration of a photoelectrochemical cell that consists of a semiconducting photoanode and a metal cathode. The corresponding energy diagram is shown on the right [9].

For an acidic environment, subtracting or adding the dissociation reaction of water into protons and hydroxyl ions, the appropriate reactions can be obtained:

$$4\,\mathrm{H^+} + 4\,\mathrm{e^-} \rightleftharpoons 2\mathrm{H_2} \quad E^0_{red} = 0.000\ V\ vs.\ NHE$$
$$2\,\mathrm{H_2O} + 4\,\mathrm{h^+} \rightleftharpoons 4\,\mathrm{H^+} + \mathrm{O_2} \quad E^0_{ox} = -1.229\ V\ vs.\ NHE$$

Both the standard electrode potentials are taken with respect to the normal hydrogen electrode (NHE), namely the potential of a platinum electrode in 1 M acid solution. Applied potentials are nowadays usually reported against the Reversible Hydrogen Electrode (RHE) scale for water splitting studies. Zero volts on the RHE scale reflect the H^+/H_2 redox potential in the actual solution, irrespective of the pH. This makes it more convenient to use than the NHE scale, for which $\phi\ (H^+/H2) = 0\ V$ only at the unit activity of the H^+ ions and the dissolved H_2 gas.
The Gibbs free energy change for the overall water-splitting reaction is given by the expression:

$$\Delta G = -nF\Delta E$$

At standard temperature (298 K) and concentrations (1 mol/L, 1 bar), the electrochemical cell voltage ΔE of $-1.229\ V$ corresponds to a Gibbs free energy change of +237 kJ/mol H_2. This shows that the water-splitting reaction is thermodynamically uphill.
The conversion of sunlight to H_2 is one of the most important developments in water splitting. Established technology splits water in two steps: a photovoltaic cell can be used to convert solar radiation into electricity which is then used to separate electrolysers to generate hydrogen from water. Photovoltaic conversion occurs with varying efficiency depending upon the semiconductor material used.
The conversion of solar energy into electricity and the water-splitting reaction can be combined

in a single process in which photon absorption creates electron–hole pairs that electrochemically split water molecules or simply exploit the photovoltaic effect to overcome the overpotential to split water.

2.2 The Photovoltaic Principles

A solar cell functions as a device that transforms light energy into electricity through the phenomenon known as the 'photovoltaic effect.' This process takes place within certain semiconducting materials, such as silicon. In this process, the semiconductor absorbs a photon, which excites an electron. This excited electron can then be harnessed and channeled into an electrical circuit through the application of built-in and external electric fields. The main component of a solar cell is the semiconductor, as this is a pivotal part of the light conversion into electricity process. Semiconductors can carry out this conversion due to the structure of their electron energy levels. A photon only needs to have energy greater than that of the band gap to excite an electron from the valence band into the conduction band.
The most commonly known solar cell is configured as a large-area p-n junction made from silicon, which is an interface between two types of semiconductor materials, p-type and n-type, inside a single crystal of semiconductor. In such a configuration, electrons can migrate from the region of high electron concentration (the n-type side of the junction) into the region of low electron concentration (the p-type side of the junction). However, in the absence of an external circuit, this diffusion of carriers cannot continue indefinitely. This is because the accumulation of charge on either side of the junction generates an electric field that opposes the further diffusion of charges. Ultimately, an equilibrium is established where the net current becomes zero, leaving a region on either side of the junction where electrons and holes have diffused across the junction and annihilated each other called the depletion region because it contains practically no mobile charge carriers. Nevertheless, if a small enough load is connected, the electrons prefer to go around the external circuit in their attempt to restore equilibrium, doing useful work on the way (Fig. 2.2).

In a solar cell, there are two causes of charge carrier motion and separation:

- Drift of carriers, propelled by the electric field, results in electrons being urged in one direction and holes in the opposite direction.
- Carriers undergo diffusion, moving from regions with a higher carrier concentration to regions with a lower carrier concentration, following a gradient of chemical potential.

These two "influences" may oppose each other within the cell. For example, when an electron travels through the junction from the p-region to the n-region (as depicted in the initial diagram in this article), it experiences a force from the electric field counteracting the concentration gradient. This same principle applies to a hole moving in the opposite direction.
The generation of current is best comprehended by considering electron-hole pairs formed

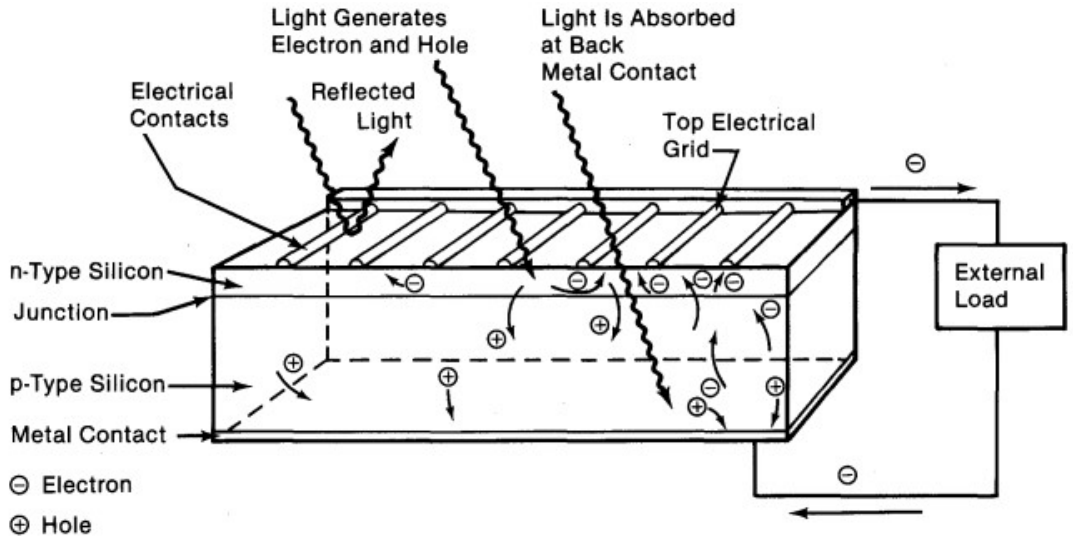

Figure 2.2: Illustration of a Photovoltaic cell. Light incident on the cell creates electron-hole pairs, which are separated by the potential barrier, creating a voltage that drives a current through an external circuit [10].

within the depletion zone, characterized by a robust electric field. The electric field drives electrons toward the n-side and holes toward the p-side. When this pair forms outside the space charge zone, where the electric field is weaker, diffusion also contributes to carrier movement. Nevertheless, the junction still has a role by directing any electrons arriving from the p-side to the n-side and guiding any holes arriving from the n-side to the p-side, thus establishing a concentration gradient outside the space charge zone.
In thick solar cells, diffusion dominates the charge separation processes, while in thinner ones, such as amorphous silicon, the diffusion length of minority carriers is usually very short due to the existence of defects, and the dominant charge separation is, therefore, drift, driven by the electrostatic field of the junction, which extends to the whole thickness of the cell [11].

2.3 The Electrode-Liquid junction

Depending on the type of electrode, it is crucial to investigate what happens at its interface with the electrolyte. In fact, when a metal oxide semiconductor is exposed to humid air, the surface undergoes hydroxylation. However, a more complex situation arises when the semiconductor is immersed in an aqueous solution. Depending on the pH of the solution, specific adsorption of protons or hydroxide species affects the charge distribution at the semiconductor/electrolyte interface, as well as the potential distribution. In this scenario, both H^+ and OH^- ions in the solution will adsorb and desorb from the surface. This dynamic equilibrium is established and relies on the solution's pH and the surface's Brønsted acidity. The pH at which the net adsorbed

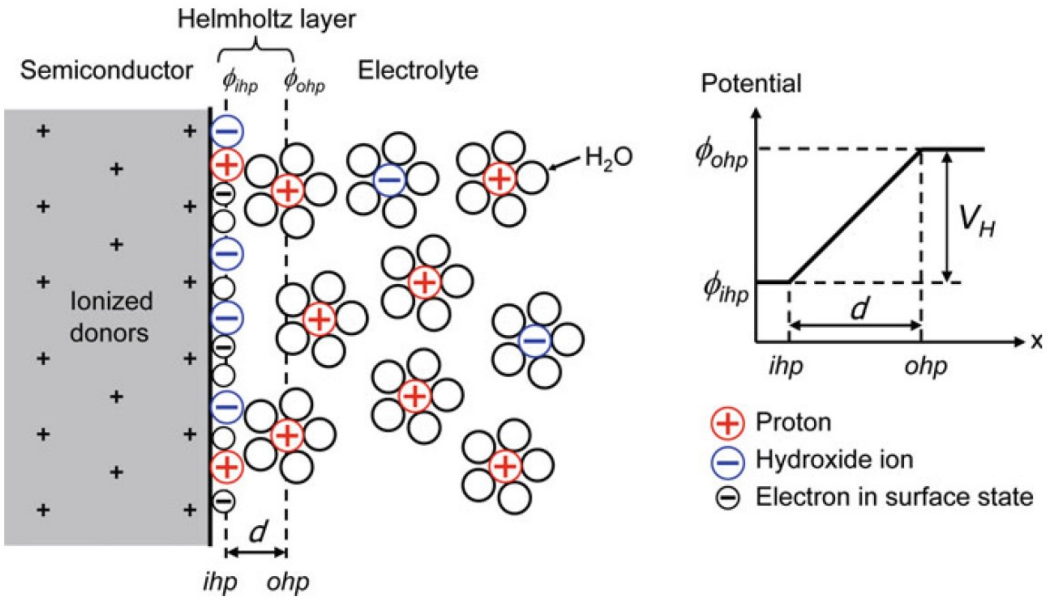

Figure 2.3: Schematic model of the semiconductor/electrolyte interface and the Helmholtz layer. The inner Helmholtz plane (*ihp*) consists of H^+ and OH^- ions that are specifically adsorbed at the semiconductor surface. The outer Helmholtz plane (*ohp*) marks the closest approach's distance for ions still in the solution. The distance d is only a few Å due to the solvation sheet of water molecules surrounding each ion [9].

charge is zero is called the *point of zero charge* (PZC) of the semiconductor.
Generally, it is important to study what happens at the surface of the electrode when in contact with an electrolyte. In a PEC device, the structure of the semiconductor/electrolyte interface is depicted in Fig. 2.3. At the surface, there are charges consisting of trapped electrons (or holes) in surface states, along with specifically adsorbed ions. The region between the specifically adsorbed ions and the closest ions in the solution is referred to as the *Helmholtz layer*, typically with a width of $\sim 2-5$ Å.
When PV cells are used in a monolithic configuration, the anode and cathode surfaces create an electrode-electrolyte junction where the two half-reactions occur: Hydrogen Evolution Reaction (HER) and Oxygen Evolution Reaction (OER). The converted electricity of the solar cells is channeled in order for the OER and the HER to happen, but, due to the significant kinetic barrier of the water-splitting process, the need of (electro-)catalysts is crucial to lower this barrier and allow the production of the gasses.

2.3.1 The Hydrogen Evolution Reaction (HER)

HER is the key half-reaction to produce hydrogen at the cathode in water electrolysis which involves a two-electron transfer process. The mechanism of this HER is highly dependent on the environmental condition. From a thermodynamic point of view, this multi-step electrode reaction should occur at the potential of the reference hydrogen electrode (RHE). In acidic media, the first step of this reaction is the reduction of a proton on an active site of the catalyst surface (Volmer step, Eq. 2.1), followed by the evolution of molecular H_2, either through a second proton/electron transfer (Heyrovsky step, Eq. 2.2) or through the recombination of two adsorbed protons (Tafel step, Eq. 2.3):

$$H_3O^+ + e^- + M \longrightarrow H_{ads} + H_2O \tag{2.1}$$

$$H_{ads} + H_3O^+ + e^- \longrightarrow H_2 + H_2O + M \tag{2.2}$$

$$2H_{ads} \longrightarrow H_2 + 2M \tag{2.3}$$

where M refers to a vacant surface site of the electrocatalyst, and H_{ads} to adsorbed hydrogen atoms.
While in the acidic solution, both the Volmer and Heyrovsky reactions involve a discharged hydronium ion, in alkaline media those two steps affect the hydroxide ion (Eq. 2.4 and Eq. 2.5), whereas the Tafel reaction stays unaltered.

$$H_2O + e^- + M \longrightarrow H_{ads} + OH^- \tag{2.4}$$

$$H_2O + e^- + H_{ads} \longrightarrow H_2 + OH^- \tag{2.5}$$

The difference between the acidic conditions and alkaline/neutral conditions is that in alkaline/neutral conditions the H_{ads} intermediates are formed by dissociation of H_2O [12].
From Sabatier's principle, the interactions between the catalyst and the substrate should be "just right"; that is, neither too strong nor too weak. If the interaction is too weak, in fact, the molecule will fail to bind to the catalyst and no reaction will take place. On the other hand, if the interaction is too strong, the product fails to dissociate. Therefore, ideally, the formed H_{ads} bonds on the electrocatalysts should be neither too weak nor too strong to facilitate the formation of H_{ads} intermediate and the release of H_2 [13]. Therefore, the free energy of hydrogen adsorption is widely accepted to be a descriptor for a hydrogen evolution material.
A moderate value of hydrogen binding energy (HBE) will benefit the HER process. As shown in Fig. 2.4, the volcano curve provides a quick comparison of the activities of different metals in acidic media and alkaline media, respectively. Platinum appears to be the best catalyst for HER in both media which have the optimal hydrogen adsorption energy showing the highest exchange current density. The activity of HER in alkaline media is usually lower than that in acidic media. This largely stems from the fact that the reaction is hindered by the sluggish water dissociation step, which leads to a reduction of the reaction rate by 2–3 orders of magnitude. However, alkaline electrolysis is preferable in industrial plants. The rational design of electrocatalysts with high alkaline HER performance requires the catalysts to have the characteristics of binding hydrogen species and dissociating water [14].

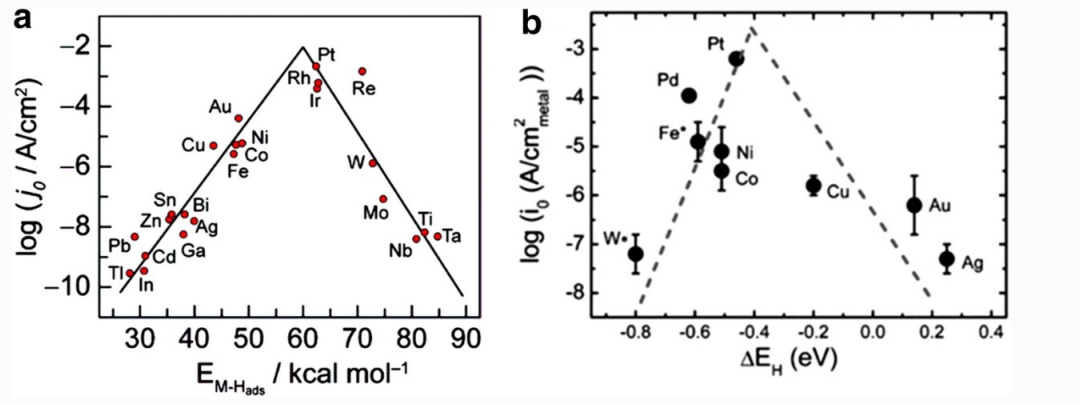

Figure 2.4: Volcano plots: a) exchange current density vs. the H_{ads} bond energy for each metal surface (for acidic media); b) exchange current density on monometallic surfaces vs. the calculated HBE (for alkaline media) [14].

2.3.2 The Oxygen Evolution Reaction (OER)

The activation energy dictating the reaction kinetics can be significantly reduced by using electrocatalysts. An important efficiency-limiting factor of alkaline water splitting is the oxygen evolution reaction (OER). The kinetics of this anodic half-reaction is much more complex compared to its counterpart: OER is triggered by multiple electron transfer steps and oxygen–oxygen bond formation, which is thermodynamically more challenging than the two-electron transfer process in HER [15].

The OER is a multiple-step reaction involving the adsorption and desorption of several different surface intermediates, for example, oxo, peroxide, and superoxide species. The initial step of OER in an alkaline electrolyte is the adsorption of a hydroxide radical at the active site of the electrocatalyst [16]. If the reactions happen solely on catalytically active transition metal sites, (M) with the electrolyte species ($OH^-/H^+/H_2O$) being the only reactants, it is called an adsorbate evolution mechanism (AEM). A simplified OER pathway on the metal sites was proposed by Song and his co-workers, as depicted in Fig. 2.5 [17] where the reactions are the following:

$$OH^- + M \longrightarrow M - OH + e^- \tag{2.6}$$

$$M - OH + OH^- \longrightarrow M - O + H_2O + e^- \tag{2.7}$$

$$2M - O \longrightarrow 2M + O_2 + 2e^- \tag{2.8}$$

$$M - O + OH^- \longrightarrow M - OOH + e^- \tag{2.9}$$

$$M - OOH + OH^- \longrightarrow O_2 + H_2O + M + e^- \tag{2.10}$$

where the sequence of reaction steps is shown by the direction of the arrows.

In the first step (Eq. 2.6), the active metal site adsorbs a hydroxide ion (OH^-) to form the initial

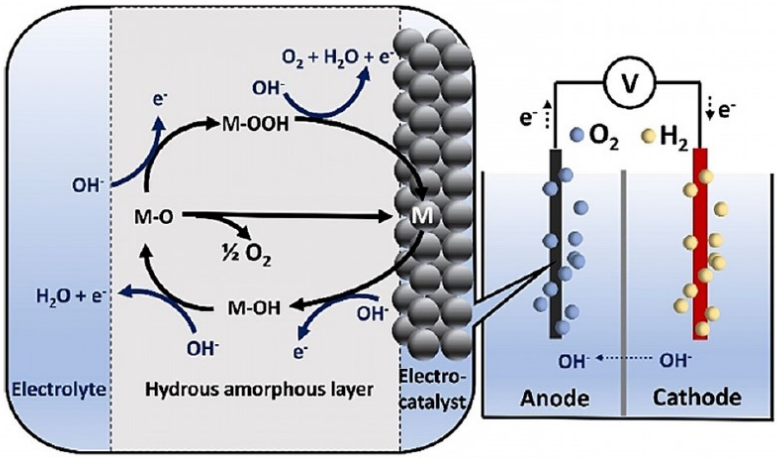

Figure 2.5: An alkaline water-splitting cell. The magnification shows a generalized mechanism of OER in the alkaline medium over a metal electrocatalyst [18].

M-OH intermediate along with the release of one electron. Another hydroxide ion reacts with the M-OH intermediate by coupling with a proton and removing an electron to form molecular H_2O and an M-O intermediate (Eq. 2.7). Two different pathways are available to produce molecular O_2 from the M-O intermediate.
The first one (Eq. 2.8), is through the direct combination of two M-O species, with a large activation barrier. The second one, which is seen as a more representative pathway, consists of two reaction steps. The first step involves the formation of an M-OOH intermediate by the nucleophilic attack of OH^- ion on the M-O intermediate, where the third electron is fed into the circuit (Eq. 2.9). Subsequently, a hydroxide ion attacks the M-OOH intermediate and forms molecular O_2, and releases the fourth electron (Eq. 2.10) [18].

The aforementioned mechanisms all involve reaction steps characterized by redox processes occurring at a metal cation site, with the electrolyte serving as the sole reactant. Nevertheless, it has been demonstrated that oxide electrocatalysts can also facilitate the Oxygen Evolution Reaction (OER) through the involvement of lattice oxygen. This mechanism is known as the lattice oxygen-mediated mechanism (LOM). The LOM concept emerged primarily due to findings from density functional theory (DFT) calculations, which demonstrated its better alignment with experimental data obtained from highly active electrocatalysts such $La_{1-x}Sr_xCoO_{3-\delta}$ [19].

Fig.2.6 illustrates the disparity between AEM and LOM within an alkaline environment using a Co-based catalyst. Two crucial distinctions set LOM apart from AEM. Firstly, LOM necessitates the involvement of lattice oxygen to facilitate the OER (I_1). Secondly, it does not alter the oxidation state of the transition metal (TM) cation. In fact, as can be seen from the partial density of states (PDOS), step 1 of the LOM is separated into an electrochemical (1E) step in which the ligand hole is generated and a chemical step (1C) in which the lattice oxygen

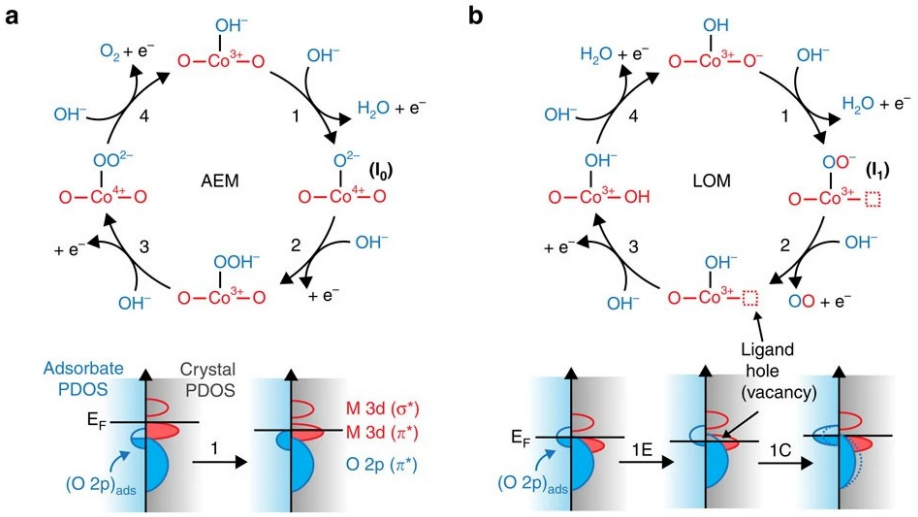

Figure 2.6: AEM (a) and LOM (b) during Oxygen Evolution Reaction in alkaline media. Lattice species are shown in red and electrolyte species are shown in blue. Partial density of states (PDOS) of the two mechanisms are given below [19].

is exchanged into the adsorbed intermediate resulting in lattice oxygen that yields a superoxide ion (O_2^-) intermediate rather than oxidizing Co to Co_4^+.
It has been observed that the choice of mechanism for mediating the OER (AEM or LOM) significantly influences the stability of the catalyst. Specifically, catalysts with an increasing contribution from LOM during the OER process tend to exhibit lower bulk stability. However, if the regeneration of lattice oxygen (steps 3 and 4) occurs more slowly than the release of lattice oxygen (steps 1 and 2), the initial surface structure of the electrocatalyst will degrade over time. This process often leads to surface amorphization, altering the pristine atomic structure of the catalyst and potentially undermining its stability [20].

2.4 The Charge Transport

The steady-state governing conservation and transport equations for both neutral and charged species were given by Nernst–Planck:

$$-\nabla \cdot \boldsymbol{N}_i + R_{r,l} = 0 \tag{2.11}$$

with

$$\boldsymbol{N}_i = -z_i \mu_{i,e} F c_i \nabla \Phi_l - D_{i,e} \nabla c_i + \boldsymbol{u} c_i \tag{2.12}$$

where $\boldsymbol{N}_i$ is the molar flux vector, R_i is the reaction source term, $\boldsymbol{u}$ is the superficial liquid velocity vector, z_i and c_i are the valence and concentration of species i, respectively, F is Fara-

day's constant, and $\mu_{i,e}$ and $D_{i,e}$ are the effective mobility and diffusivity of species i, respectively, and F_l is the potential of the liquid phase. The values of $\mu_{i,e}$ and $D_{i,e}$ are related by the Nernst–Einstein relationship for charged species,

$$\mu_{i,e} = \frac{D_{i,e}}{RT} \tag{2.13}$$

"Effective" refers to non-bulk properties accounting for multi-phase media such as separators or porous electrodes.

The use of Eq. 2.12 assumes dilute-solution theory, in which the interactions among the solutes are not rigorously considered. It is general for the ionic species of concern (i.e. H^+ and OH^- and their counterions) and simplifies the convection-diffusion equation for the dissolved neutral species (i.e. H_2 and O_2) where $z_i = 0$. The velocity term accounts for fluxes resulting from convective flow due to a pressure gradient, which were determined by solving the mass and momentum (laminar flow) conservation equations,

$$\nabla \cdot \boldsymbol{u} = 0 \tag{2.14}$$

$$\frac{\rho}{\epsilon}\boldsymbol{u} \cdot \nabla \frac{\boldsymbol{u}}{\epsilon} = -\nabla p + \frac{\mu}{\epsilon}\Delta \boldsymbol{u} - \frac{\mu}{K}\boldsymbol{u} \tag{2.15}$$

where ρ is the density, ϵ is the porosity, p is the pressure, μ is the viscosity, and K is the permeability. The last term on the right side of the momentum conservation equation, Eq. 2.15, is the Darcy extension which accounts for viscous resistances due to the presence of porous media and tends to zero for a continuous fluid phase for which K is large.

The transport of charge and subsequent calculation of the potential losses were determined by the definition of the current density,

$$\boldsymbol{i}_l = F \sum_i z_i \boldsymbol{N}_i \tag{2.16}$$

where the subscript l (liquid) denotes the ion-conducting phase. If the current losses due to concentration gradients are neglected, by the use of electroneutrality, the latter equation results in Ohm's law:

$$\boldsymbol{i}_l = \frac{F^2}{RT}\nabla\Phi_l \sum_i z_i^2 D_{i,e} c_i = \kappa_{l,e}\nabla\Phi_l \tag{2.17}$$

where $\kappa_{l,e}$ is the effective solution or electrolyte conductivity, expected to be constant for a well-stirred or continuously flushed reactor.

Similarly, Ohm's law governs the transport of charge in the solid, electron-conducting phase,

$$\boldsymbol{i}_s = -\sigma_{s,e}\nabla\Phi_s \tag{2.18}$$

where the subscript s (solid) denotes the electron-conducting phase. For conservation of charge,

$$\nabla \cdot \boldsymbol{i}_s = -\nabla \cdot \boldsymbol{i}_l = A_0 i_R \tag{2.19}$$

where i_R is the reaction or transfer current between the ionic and electronic phases and A_0 is the specific surface area.
The transfer current depends on the electrochemical reaction kinetics, which is expressed by the use of Butler-Volmer expressions for the oxygen evolution reaction OER (hydrogen evolution reaction HER):

$$i_R^{OER} = i_0^{OER} \left[\left(\frac{c_{red}}{c_{red,0}} \right)^{\gamma_{red}} exp\left(\frac{\alpha_a^{OER} F \eta_{op}}{RT} \right) - \left(\frac{c_{ox}}{c_{ox,0}} \right)^{\gamma_{ox}} exp\left(\frac{-\alpha_c^{OER} F \eta_{op}}{RT} \right) \right] \tag{2.20}$$

where i_0^{OER} (i_0^{HER}) is the OER (HER) exchange current density, η_{op} is the overpotential, and $\alpha_{a,i}$ and $\alpha_{c,i}$ are the OER (HER) anodic and cathodic transfer coefficients, respectively. The concentration terms in the kinetic equations are unity for a well-stirred, or continuously flushed reactor [21].

2.5 The Photoelectrochemical Cell under Operating Conditions

The analysis of the system and its energy diagram is conducted under illumination. Fig. 2.7 depicts the energy diagram of a PEC cell under dark and light conditions. In the absence of light, the H_2O/O_2 redox couple is assumed to be the predominant species, dictating the electrochemical potential of the solution. The Fermi levels of the semiconductor and the electrically connected metal, adjust to a value in close proximity to E_{ox}. However, upon illumination, the generation of electron-hole pairs leads to an increase in the Fermi level by ΔV_{photo}, which represents the internal photovoltage. Since the system is no longer in equilibrium, particularly within the SCR where the electrons and holes are generated, the use of a single Fermi level is no longer suitable.
Instead, the concept of *quasi-Fermi levels* is employed. These levels directly indicate the concentration of electrons and holes at a specific location x within the semiconductor and are defined as follows:

$$n = n_0 + \Delta n = N_C e^{-\left(E_C - E_{F,n}^*\right)/kT} \tag{2.21}$$

$$p = p_0 + \Delta p = N_V e^{-\left(E_{F,p}^* - E_V\right)/kT} \tag{2.22}$$

where n_0 and p_0 are the equilibrium carrier concentrations in the dark, and Δn and Δp are the additional carriers created by illumination.
For an n-type semiconductor, $n = n_0 + \Delta n \approx n_0$ and $p = p_0 + \Delta p \approx p_0$ so that $E_{F,n}^*$ remains horizontal whereas $E_{F,p}^*$ departs from the bulk Fermi level in the active region, as can be seen in the right side of Fig.2.7.
One particular aspect to be noted is that the quasi-Fermi level definitions in Eq. 2.21 and Eq. 2.22 only consider electrons and holes in the conduction and valence bands. They do not

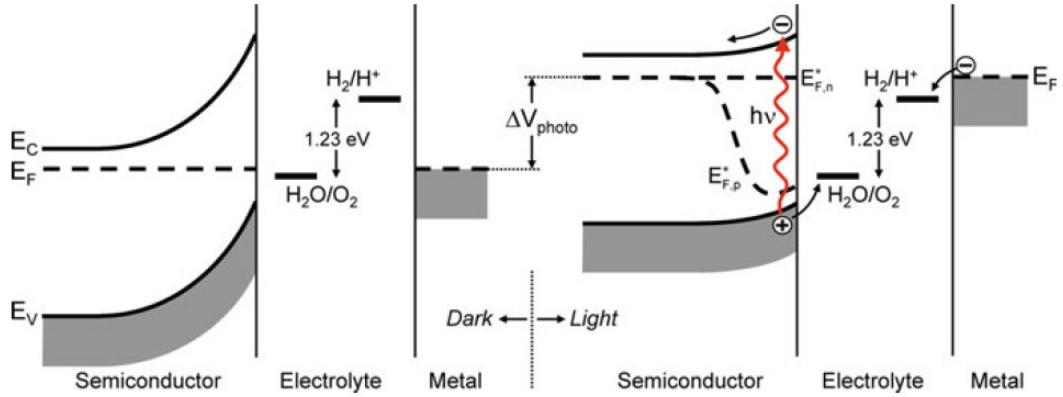

Figure 2.7: Band diagram for a PEC cell based on an n-type semiconducting photoanode that is electrically connected to a metal counter electrode; in equilibrium in the dark (*left*) and under illumination (*right*). Illumination raises the Fermi level and decreases band bending. Near the semiconductor/electrolyte interface, the Fermi level splits into quasi-Fermi levels for the electrons and holes [9].

account for any changes in the occupation of surface or bulk defect states, which limits their predictive value for reactions in which these states are involved.

2.5.1 Photocurrent-Voltage Characteristics

One of the most used models to describe theoretically the semiconductor photocurrent-voltage characteristics was reported by Gärtner [22], who derived for a semiconductor under reverse bias:

$$j_G = j_0 + e\Phi\left(1 - \frac{e^{-\alpha W}}{1+\alpha L_p}\right) \tag{2.23}$$

where Φ is the incident light flux, α is the absorption coefficient (assuming monochromatic illumination), W is the depletion layer width, L_p is the hole diffusion length, and j_0 is the saturation current density. The model assumes that there is no recombination in the SCR and at the interface.
An improved model was proposed by Reichman [22], where an important role is played by the saturation current density,

$$j_0 = \frac{eL_p N_C N_V}{\tau N_D} e^{(-E_g/kT)} \tag{2.24}$$

here E_g is the energy gap, τ is the minority carrier lifetime, N_C, N_V, and N_D are the density concentration of electrons, holes, and donors, respectively.
In this model, the derivation of the total valence band photocurrent in an n-type semiconductor

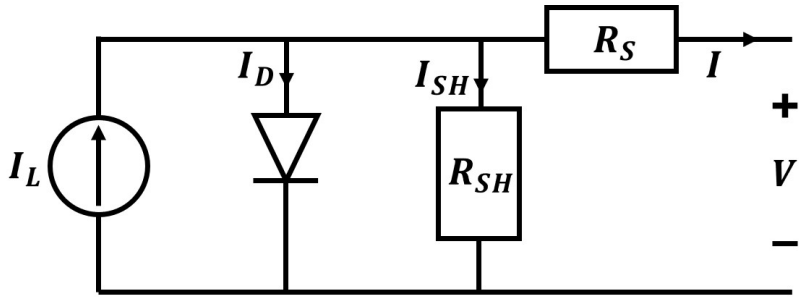

Figure 2.8: Equivalent circuit of a solar cell.

is obtained by considering more appropriate boundary conditions:

$$j_V = \frac{j_G - j_0 e^{-(e\eta/kT)}}{1 + \frac{j_0}{j_V^0} e^{-(e\eta/kT)}} \tag{2.25}$$

Here, j_V^0 is the hole transfer rate at the interface, and j_0 is the saturation current density, i.e., the hole current in the valence band at $x = W$ when $\Phi = 0$. The overpotential η, is defined as the difference between the applied potential and the open-circuit potential when the system is illuminated. Reichman's model considers the possibility of recombination occurring within the SCR, which becomes significant when the photovoltage is sufficiently high to flatten the energy bands. In the case where the bandgap exceeds ∼1.8 eV, as is the case for most metal oxides, j_0 becomes negligible. Consequently, Eq. 2.23 and Eq. 2.25 yield nearly identical results.
As for the photovoltaic case, it is useful to create a model which is electrically equivalent. An ideal solar cell may be modeled by a current source in parallel with a diode; in practice no solar cell is ideal, so a shunt resistance and a series resistance component are added to the mode, as depicted in Fig. 2.8.

From the equivalent circuit it is evident that the current produced by the solar cell is equal to that produced by the current source, minus that which flows through the diode, minus that which flows through the shunt resistor:

$$I = I_L - I_D - I_{SH} \tag{2.26}$$

where I is the output current, I_L, I_D, and I_{SH} are the photogenerated, the diode, and the shunt ones, respectively. Considering V_j as the voltage across both the diode and the resistor R_{SH}, and V_T as the thermal voltage equal to kT/q, using the Shockley diode equation, the current diverted through the diode can be obtained:

$$I_D = I_0 \left[\exp\left(\frac{V_j}{nV_T} \right) - 1 \right] \tag{2.27}$$

where I_0 is the reverse saturation current, n is the diode ideality factor.
By considering Ohm's law in the shunt resistor, and substituting in Eq. 2.26, the characteristic equation of a solar cell, which relates solar cell parameters to the output current and voltage is achieved:

$$I = I_L - I_0 \left[\exp\left(\frac{V + IR_S}{nV_T} \right) - 1 \right] - \frac{V + IR_S}{R_{SH}} \tag{2.28}$$

Since the changes in the currents are the dominating ones and are balancing each other, the open-circuit voltage (V_{OC}), when the cell operates at zero current, is practically the same; V_{OC} starts to depend on the cell size only if R_{SH} becomes too low. To account for the dominance of the currents, the characteristic equation is frequently written in terms of current density, or current produced per unit cell area:

$$j = j_L - j_0 \left[\exp\left(\frac{q\left(V + jr_S\right)}{nkT} \right) - 1 \right] - \frac{V + jr_S}{r_{SH}} \tag{2.29}$$

where all the previous currents are density currents now (A/cm^2), and the resistances are specific resistances ($\Omega \cdot cm^2$).

2.6 Energy and Quantum Conversion Efficiencies

Energy conversion efficiency plays a crucial role in evaluating the performance of a PV-PEC cell. It serves as a key metric to measure the effectiveness of converting solar energy into hydrogen. Assuming that all the electrons and holes generated by the illumination are utilized for the water-splitting process, the overall solar-to-hydrogen efficiency can be expressed as follows:

$$\eta_{STH} = \frac{P^{out}_{electrical} - P^{in}_{electrical}}{P_{light}} = \frac{j_{photo}\left(V_{redox} - V_{bias}\right)}{P_{light}} \tag{2.30}$$

V_{redox} is usually taken to be 1.23 V (at room temperature), based on a Gibbs free energy change for water-splitting of 237 kJ/mol. The enthalpy change (286 kJ/mol corresponding to a redox potential of 1.48 V) is used when the hydrogen produced will be used in a combustion process, whereas the former value is more appropriate when the hydrogen is converted into electricity in a fuel cell [23].
Assuming AM 1.5 G incident sunlight ($P_{light} = 1000\ W/m^2$) and no applied bias, the efficiency can be directly evaluated from the photocurrent as $\eta_{STH} = 1.23 \times j_{photo}$, where the efficiency is expressed in % and the photocurrent in mA/cm^2. It should be emphasized that V_{bias} refers to the actual potential difference between the working and counter electrodes.
In addition to the STH efficiency, the Faradic efficiency η_F should also be considered. It represents the ratio between the experimentally detected amount of the objective gas and the amount of gas theoretically generated [24]. Due to the secondary reactions occurring on the electrode,

η_F is typically less than 100%. However, in water electrolysis, hydrogen is produced with a purity exceeding 99%, indicating that gas purity issues are primarily associated with the cell membrane permeation rather than Faradic losses at the electrodes.
Alternatively, the solar-to-hydrogen efficiency can be determined by measuring the evolved hydrogen using techniques such as mass spectrometry, gas chromatography [25, 26], or by monitoring the water displacement in an inverted burette.
The STH efficiency for this method is calculated as follows:

$$\eta_{STH} = \frac{\Phi_{H_2} G^0_{f,H_2}}{P_{light}} \tag{2.31}$$

where Φ_{H_2} is the rate of H_2 evolution at the illuminated area ($mol/s/m^2$) and G^0_{f,H_2} is the Gibbs free energy of formation of hydrogen (237 kJ/mol).
When reporting STH efficiencies, it is crucial to ensure that the water-splitting reaction is stoichiometric ($H_2 : O_2 = 2 : 1$), with no other reactions occurring, and that the light source is well-specified and closely matches the intensity and spectral distribution of the AM 1.5G spectrum.
In the quest to identify performance-limiting factors in PEC photoelectrodes, quantum efficiency as a function of wavelength is a particularly useful parameter. The *external quantum efficiency*, known as IPCE (*Incident Photon-to-current Conversion Efficiency*), measures the fraction of incident photons that are converted to measurable electrons in the outer circuit. It is defined as:

$$IPCE(\lambda) = \frac{hc}{e}\left(\frac{j_{photo}(\lambda)}{\lambda P(\lambda)}\right) \tag{2.32}$$

Another valuable parameter is the APCE, or *Absorbed Photon-to-current Conversion Efficiency*. In contrast to the IPCE, the APCE also corrects for reflection losses, and it is often referred to as *internal quantum efficiency*, related to the IPCE via

$$APCE(\lambda) = \frac{IPCE(\lambda)}{1 - R - T} \tag{2.33}$$

where R and T are the optical reflection and transmission, respectively. During steady-state operations, the photocurrent is integrally linked to the hydrogen-producing performance of the PEC system. Considering the PEC half-reactions in Sec.2.26, it is known that two electrons are consumed in the evolution of one H_2 molecule. Consequently, the hydrogen production rate is half the rate of electron flow, which is equivalent to half the photocurrent:

$$R_{H_2} = \frac{I_{ph}}{2e} = \frac{J_{ph} \times A}{2e} \tag{2.34}$$

where R_{H_2} is the hydrogen production rate (s^{-1}), I_{ph} is the photocurrent, A is the area of the illuminated photoelectrode, and J_{ph} corresponds the photocurrent density.

Chapter 3

State of the Art Devices: from Single- to Multi-junctions

Solar-powered water-splitting, specifically through photoelectrochemical (PEC) water-splitting using semiconductor photoelectrodes or photocatalysts, is considered one of the most promising approaches for large-scale renewable hydrogen production with minimal carbon emissions. Despite its potential, the development of stable and efficient PEC materials, devices, and systems poses significant challenges, making it an ongoing pursuit. However, it has to be kept in mind that the conversion of sunlight to practical end-uses is inevitably constrained by inherent losses associated with energy conversion pathways. Each additional step in the conversion process introduces losses and diminishes the overall efficiency of conversion. Therefore, while solar-powered water-splitting holds great promise, it is crucial to address and mitigate these energy losses to maximize the overall conversion efficiency.

3.1 Single Junction PEC Semiconductor Device

In a semiconductor-based PEC system, the absorption of photons occurs within the semiconductor, leading to the generation of charge carriers that are subsequently separated and then extracted through interfacial HER and OER reactions. In photoelectrode-based systems, charge separation primarily relies on the rectifying nature of the semiconductor/electrolyte junction. While the specifics of charge separation may differ in photocatalyst systems [27], the fundamental mechanisms of absorption and extraction at the solid/liquid interface remain the same. In both cases, the hydrogen production performance is strongly influenced by both the semiconductor material properties and the interfacial characteristics.
In PEC photoelectrode systems, the semiconductor/electrolyte interface can form a rectifying junction, similar to the solid-state *pn* junctions or Schottky diode junctions used in solar cells. These rectifying junctions possess built-in electric fields capable of effectively separating the photogenerated charge carriers produced within the semiconductor bulk upon photon absorp-

tion. In PV cells, this charge separation mechanism drives photocurrents for electricity production, whereas in PEC systems, the charge separation facilitates the HER and OER half-reactions for water splitting. In both scenarios, when illuminated, additional photoexcited electron–hole pairs are generated, and their separation and extraction are crucial to prevent recombination and ensure their effective participation in the energy conversion process [28].

3.1.1 Photoelectrode Junction Formation

According to Gerischer's model, the formation of a rectifying photoelectrochemical (PEC) junction at the semiconductor/electrolyte interface closely resembles the characteristics of solid-state junctions [29]. Photoanodes using n-type semiconductors form PEC junctions similar to a Schottky barrier or an np^+ junction, where internal electric fields facilitate the migration of photogenerated holes towards the electrolyte interface, promoting oxygen evolution. On the other hand, the formation of the p-type photocathode junction is analogous to a solid-state pn^+ device, where internal fields facilitate the injection of photogenerated electrons at the interface to drive the HER [30].
In Fig. 3.1 (i), the thermal equilibrium of the n-type semiconductor and electrolyte before contact is depicted for the photoanode case. At equilibrium, the Fermi level in the semiconductor (F_n) is close to the conduction band (C_B), while the Fermi level in solution (F_s) falls between the redox levels for hydrogen reduction (H^+/H_2) and water oxidation (H_2O/O_2).
Upon contact, the Fermi levels of the electrode and electrolyte align to establish thermal equilibrium, as shown in Fig. 3.1 (ii). Since the initial electrode's Fermi level is higher than that of the electrolyte, free electrons in the n-type semiconductor migrate to the solid-liquid interface, exposing positively charged fixed donor sites. The electrons create a surface charge layer at the interface, inducing a thin Helmholtz double layer in the electrolyte.
A depletion region, also referred to as a *space-charge region* (SCR), is formed where the diffusion of the free charge carrier is counter-balanced by the built-in electric field generated by the fixed charges flanking the junction. Fig. 3.1 (iii) illustrates the charge distributions, including the fixed space charges in the solid-state electrode and the Helmholtz layer charges in the solution. Typically, Helmholtz layers have a thickness on the order of a few nanometers, while the semiconductor space-charge region spans several micrometers.
The thermal equilibrium is disrupted when exposed to light, and the operations under illumination need to be described using "quasi-equilibrium" statistics, which generally remain valid for AM 1.5G solar irradiance and moderate levels of concentrated sunlight [28].

3.1.2 Illuminated Response

Under illumination, the electron-hole pairs generated through photon absorption near the space-charge regions can be separated by the built-in electric fields. In the photoanode case, the photogenerated holes are driven towards the electrolyte interface by the built-in field, where they

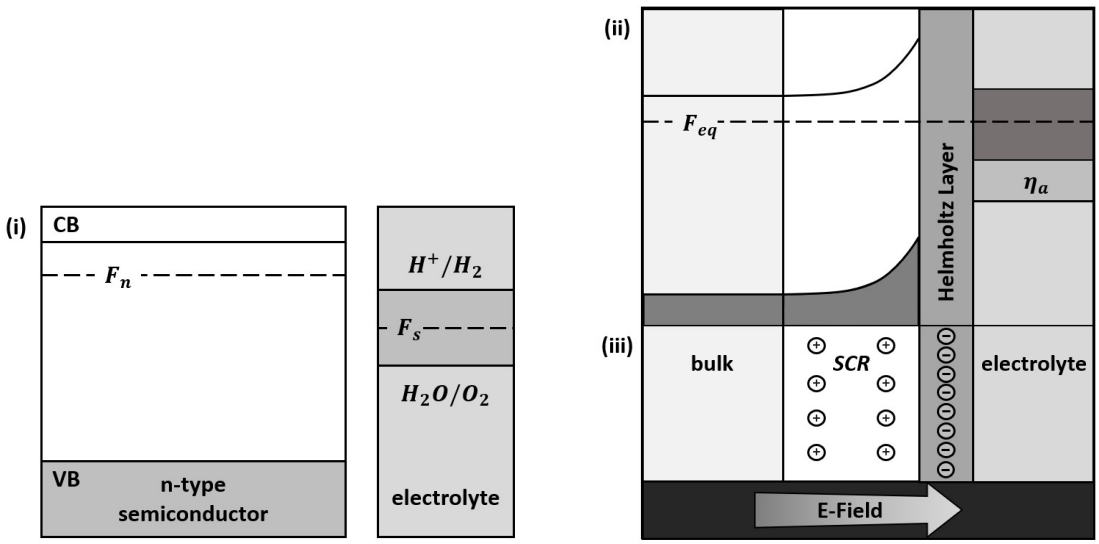

Figure 3.1: Semiconductor/electrolyte junction formation for an n-type semiconductor and junction. Subheadings (i), (ii), and (iii) represent the energy diagrams before contact, the energy diagrams after contact, and the charge distributions, respectively [9].

can facilitate the OER oxidation reaction. Simultaneously, the photoexcited electrons are directed towards the electrode's back contact, where they can be extracted into the solution at counter-electrode surfaces, appropriately conditioned to promote the HER.
Fig. 3.2 provides an illustration of the PEC junction response to solar illumination for photoanodes using the quasi-Fermi level descriptions. The photoelectrode is immersed in a solution, and the back contact is connected to a counter electrode in the same solution through external wiring. Additionally, the overpotentials η_a and η_c for the OER and the HER in solution are included, representing the additional voltage required to sustain water splitting.
Upon sunlight absorption in the semiconductor bulk, the original Fermi levels split into separate quasi-Fermi levels for electrons (F_e) and holes (F_h) resulting from the excess concentration of photogenerated electron-hole pairs compared to the equilibrium populations.
In the photoanode case, the excess hole population significantly alters the distribution of minority carriers compared to the equilibrium, while the excess electrons have a negligible effect on the majority carrier populations. Consequently, the quasi-Fermi level for holes undergoes a substantial shift, whereas the quasi-Fermi level for electrons changes insignificantly. The opposite behavior is observed in the case of a photocathode. Near the back contact, away from the effects of illumination, the two quasi-Fermi levels converge back to the bulk equilibrium Fermi level.
The back contact potential is linked to the potential of the counter electrode, which, under operating conditions, is connected to the back half-reaction. A crucial result is that the quasi-Fermi separation in the semiconductor determines the useable energy for driving the front half-

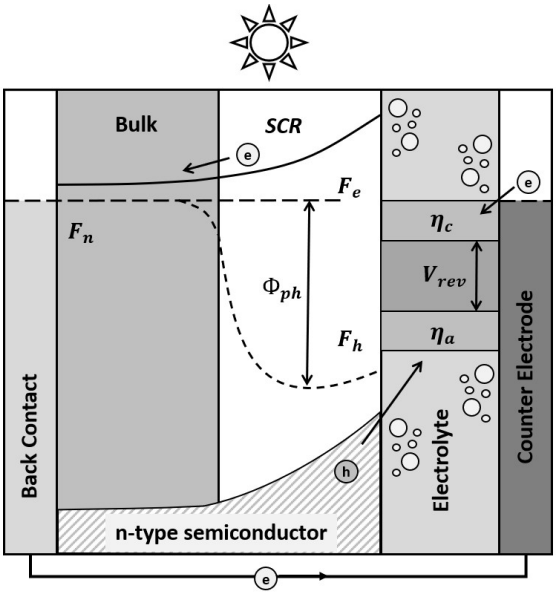

Figure 3.2: Operational illuminated PEC n-type junction with correct hole energy alignment for oxygen evolution and electron energy alignment for hydrogen production [9].

reaction. In the illuminated photoanode device shown in Fig. 3.2, the electron potential at the counter electrode is sufficiently high to drive the hydrogen reduction half-reaction, accounting for the η_c loss. Simultaneously, the quasi-Fermi hole energy at the solution interface is sufficiently low to drive water oxidation, accounting for the η_a loss. As a consequence, this configuration is capable of sustaining the net PEC water-splitting process driven by the useable energy in the quasi-Fermi split.

The concept of the quasi-Fermi level split is extremely important in determining the useable photopotential generated by a semiconductor device, particularly in relation to the bandgap energy. Thermodynamically, semiconductor band diagrams represent the internal energy of electrons and holes rather than the useable energy.

For a PEC device to be effective, its usable potential must be sufficiently high to drive both half-reactions while accounting for overpotential losses. Typically, this requirement necessitates a potential of over 1.6–1.9 V. Achieving such potential in a single junction device often requires semiconductor bandgaps exceeding 3.0 eV. However, this severely restricts optical absorption, saturated photocurrent, and ultimately the STH conversion efficiency.

Interestingly, two non-operational illuminated PEC single junctions, which alone are incapable of effectively photo-split water, can be theoretically combined in tandem to achieve the necessary usable potential for water splitting. This utilization of multiple junctions to enhance the useable photopotential represents a powerful approach for PEC water-splitting. Nevertheless, it is important to acknowledge that this strategy introduces additional system losses, which could potentially limit the overall STH efficiency.

3.1.3 Ohmic and Crossover Losses

The potential losses in the electrolyte, resulting from ion transport, play a crucial role in determining the potential drop between the anode and cathode, including losses through the separator. These losses are quantified as an average resistive solution loss

$$\Delta\Phi_R = \frac{1}{A_a}\int_{A_a}\Phi_l(x)dA - \frac{1}{A_c}\int_{A_c}\Phi_l(x)dA \tag{3.1}$$

where $\Delta\Phi_R$ is the area-averaged difference of the electrolyte potential at the same horizontal position away from the separator along the anode and cathode, respectively. The maximum potential drop due to solution resistance occurs between the centers of the electrode. This poses a limitation for actual photoelectrodes because the current drawn at the center is reduced as the difference increases, following the diode-shaped current-potential relationship of the photoelectrode.
Typically, an upper limit of 100 mV is set for the resistive potential drop $\Delta\Phi_R$, resulting in a minimal photovoltage requirement of approximately 1.65 V (1.23 V equilibrium potential, ~80 mV HER overpotential, ~220 mV OER overpotential, and 100 mV electrolyte losses).
Crossover losses, on the other hand, are influenced by the species present in the electrolyte mixture and the recombination processes. These losses determine the fraction of produced fuel that is not harvested far from the electrodes. The Faradaic yield for hydrogen collection, based on the normalized net reaction current, is used to quantify this loss.

$$\eta = \frac{\int_{A_{a/c}} i_R dA - \int_{A_{sep}} nF N_{H_2} dA}{\int_{A_{a/c}} i_R dA} \tag{3.2}$$

where the normal (reaction) current density, $i = \boldsymbol{i}\cdot\hat{\boldsymbol{n}}$, and the normal hydrogen molar flux, $N_{H_2} = \boldsymbol{N}_{H_2}\cdot\hat{\boldsymbol{n}}$, are interrelated by Faraday's law $N = i/nF$.
Crossover can occur either by diffusion through the electrolyte and/or separator, or by convection. Convective fluxes develop due to system design and control, as well as due to the natural pressure gradient that arises from the $2:1$ $H_2 - O_2$ stoichiometry of water electrolysis if the system is not actively monitored and controlled [21].

3.1.4 Loss Minimization and Efficiency Limits

PEC devices and systems experience various losses that can limit the efficiency of STH conversion, necessitating their minimization. These losses occur in the solution, at interfaces, and within the semiconductor bulk. Optoelectronic losses in the semiconductor photoelectrode, for instance, should be minimized. Large bandgap semiconductors exhibit poor absorption and generate little photocurrent, while small bandgap semiconductors suffer from high thermalization losses, leading to low conversion efficiencies. Defects present in the bulk or at the interface negatively impact the separation fields and impede charge transport.

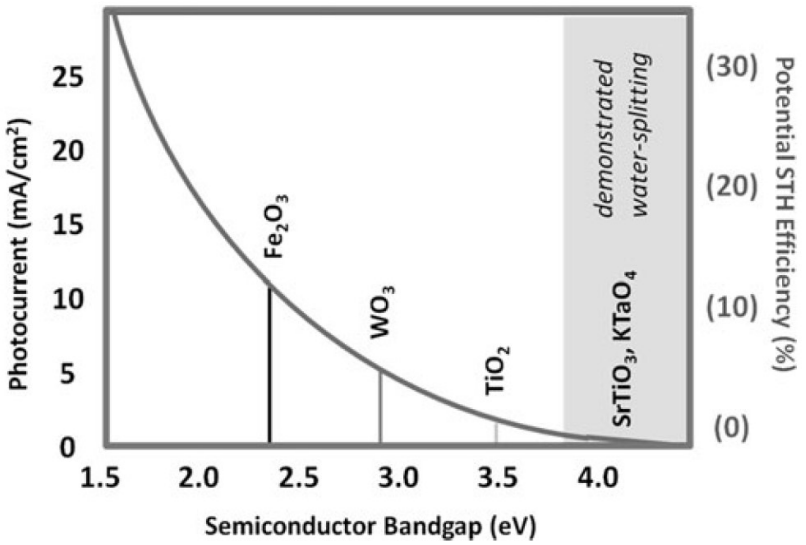

Figure 3.3: Maximum achievable photocurrent density levels and potential solar-to-hydrogen conversion efficiencies for single-junctions as a function of bandgap based on optical absorption limits. Highlighted are the high-bandgap materials that have demonstrated spontaneous PEC water splitting but at correspondingly low efficiencies [9].

To minimize overpotential losses from interfacial charge extraction and electrochemical product formation, optimization of interface conditions is crucial. The presence of parasitic or corrosion reactions that compete with the water-splitting reactions can cause significant losses. One approach to address this is the incorporation of nanoparticle catalysts on the surface, although precautions should be taken to prevent light blockage by these particles.
The electrolyte is an important factor in determining stability, the efficiency of charge-extracting reactions, and the formation of electrochemical byproducts. During PEC water-splitting, efficient removal of evolved hydrogen or oxygen gas from the photoelectrode surface is essential to minimize mass-transport losses in surface reactions and to minimize adverse optical effects. Ionic conductivity losses are often a major concern in the solution. Higher electrolyte concentrations can be employed to mitigate this issue, but this comes at the expense of increased corrosiveness.
In summary, the critical condition for PEC hydrogen production is that the quasi-Fermi levels, under solar illumination, generate sufficient useable photopotentials to drive the redox reactions involved in water splitting.

Achieving high STH conversion efficiencies for single-junction PEC photoelectrode systems, with their inherent electrochemical and solid-state losses, is challenging. The trade-off between photopotential and photocurrent due to the bandgap presents a significant hurdle for single junctions. Even with high-quality semiconductor materials, the quasi-Fermi level sepa-

ration can only reach 50–70% of the bandgap level [31].
As hydrogen production levels increase, system losses also escalate, including the current-dependent surface overpotentials, as well as electrical and ionic conductivity losses. This necessitates even higher bandgaps. The upper limit for STH conversion efficiency can be established based on the semiconductor bandgap and fundamental optical absorption limits [32], as depicted in Fig. 3.3.
Under ideal conditions, the thermodynamic single-junction limit, accounting for thermalization losses but without considering overpotential losses, is estimated to be around 30% STH. More comprehensive analyses, incorporating overpotential losses along with optical and thermalization losses, suggest that the best single junction PEC cells for AM 1.5G water-splitting are likely to be limited to STH efficiencies below 12%, even when employing the highest quality semiconductor and catalyst materials presently available [33].

3.2 Multijunctions

The use of multijunction approaches plays a pivotal role in achieving high photovoltaic conversion efficiency, serving as the foundation for current technologies for space applications and a key element in the development of future *Third Generation* PV devices. By integrating multiple junctions in stacked solar cells, the absorption of photons across the solar spectrum is significantly enhanced [34].
Similarly, in PEC solar conversion devices, the utilization of multijunction configurations can boost efficiencies by improving spectral absorption. Furthermore, multijunction PEC devices have the potential to generate higher photopotentials, meeting the voltage demands of water-splitting. However, there are trade-offs to consider, such as reduced photocurrent impacting hydrogen production rates and increased device complexity. Consequently, the design of a PEC multijunction device must strike the right balance to maximize STH conversion efficiency while managing cost considerations.

3.2.1 Multijunction Stacks and Optical Considerations

In stacking multiple cells, each one of them represents an independent photoconverting junction, such as a semiconductor *pn junction*, or a semiconductor/electrolyte PEC junction. These cells are electrically and optically connected in a series configuration. Sunlight incident on the "top" cell is partially absorbed, generating a photovoltage and photocurrent. The remaining filtered light reaches the "middle" cells, where additional absorption and photoconversion occur. Any remaining sunlight can be absorbed and converted in the "bottom" cell, as depicted in Fig. 3.4.
Since the cells are connected in series, the individual photovoltages add up, but the net current is limited by the lowest photocurrents among the cells. This is because the overall current in the

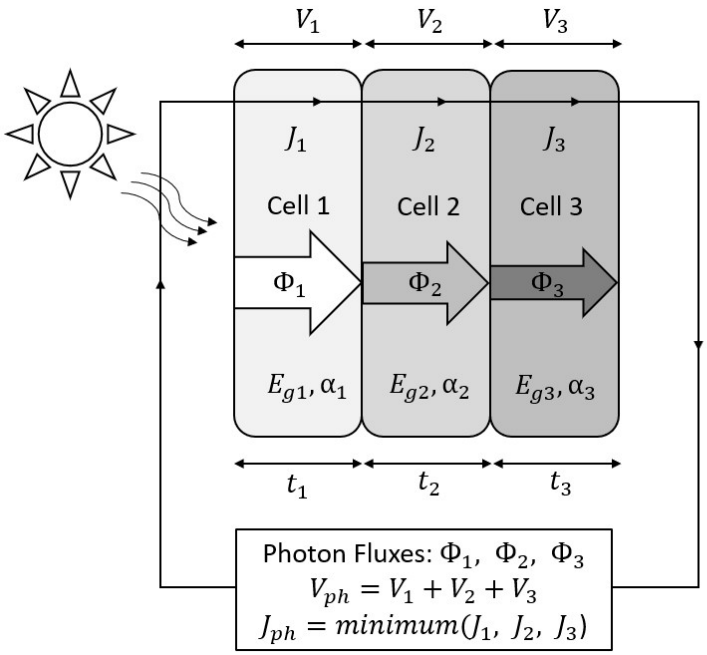

Figure 3.4: General schematic of a three-cell stack of three absorber materials with bandgap E_g and absorption coefficient α. Indicated are the photon fluxes in each cell (Φ), along with the generated photovoltages (V) and photocurrent densities (J). The total voltage in the series-connected stack is the sum of the individual cell voltages, while the stack current is the minimum of the individual cell currents [9].

device must remain continuous and is bottlenecked by the cell with the minimum current. Any excess carrier generation in the other cells will be lost internally to recombination. Since each cell operates at reduced photocurrents compared to full-sun levels, particularly the buried cells, the overall device current is diminished due to this bottleneck effect. As a result, a multijunction device based on a specific semiconductor material system generates lower photocurrent compared to a single-cell device using the same material. In general, multijunction devices offer higher voltage at the expense of lower current.

In multijunction devices, different semiconductors are selectively sensitized to different parts of the solar spectrum based on their optoelectronic properties, including bandgap and absorptivity. The macroscopic light absorption process in the material follows the Beer-Lambert Law [35], here expressed as a function of photon wavelength, λ:

$$I_\lambda(x) = I_{0,\lambda} e^{-\alpha_\lambda x} \tag{3.3}$$

where for each photon wavelength, $I_{0,\lambda}$ is the intensity of the incident flux (W/m^2), α is the absorption coefficient (m^{-1}), and x is the length of the optical pathway through the material (m). Therefore I_λ is the unabsorbed flux intensity emerging out the back of the material.

A crucial aspect of multijunction device design is the ability to tailor photon absorption and photocurrent generation in each component cell by selecting semiconductors with specific bandgap and absorption properties. The cell thickness can also be adjusted to control the optical pathway length, according to the Beer-Lambert law.
Another important parameter in characterizing the optoelectronic response of a photoactive semiconductor device is the *quantum efficiency* (QE) (more precisely, the external quantum efficiency or EQE), which plays a vital role in both single-junction and multijunction device designs because it is closely related to the absorption coefficient. Maximizing the available flux is essential, where minimizing reflection at the front surface and interfaces while optimizing back-surface reflections to redirect light back through the device can significantly enhance efficiency.
In practical multijunction designs, achieving maximum current requires "current-matching" among the individual cells in the stack [36]. By equalizing the junction currents, recombination losses are minimized, and the net current is maximized. A common approach involves stacking semiconductors with decreasing bandgaps. The top layers absorb higher energy photons while transmitting lower energy photons, which are absorbed by the subsequent layers of the device. The thickness of each cell can be adjusted to control the number of absorbed photons and fine-tune the photocurrent. To fully exploit the efficiency benefits of multijunctions devices, all interface losses must be minimized.
In the PEC junction case, additional material challenges arise due to the specific requirements for water splitting, including the potential and band-edge alignment, as well as stability in the solution.

3.2.2 PEC Multijunction Design

Multijunction device designs offer the potential to improve solar-to-electricity conversion efficiency by combining PV cells or integrating PV and PEC cells for enhanced solar hydrogen production through water splitting. The stacked junctions in these designs can provide advantages, such as increased photovoltage and expanded solar absorption range. However, the trade-off is increased device complexity and cost. In the PEC case, there is an additional trade-off of reduced photocurrent, which limits hydrogen production rates. To justify the use of multijunctions, it is essential to find the right balance between maximizing conversion efficiency and minimizing costs.
Specifically for PEC component cells, which can serve as photoanodes (OER electrodes) or photocathodes (HER electrodes) within a multijunction stack, there are additional considerations. The best-performing PEC tandem devices based on high-quality III-V crystalline semiconductors, known as "First Generation" devices, have achieved STH conversion efficiencies exceeding 10%. However, these devices suffer from limitations in long-term stability and affordability. More stable and affordable "Second Generation" thin-film PEC multijunction devices have been demonstrated, but their performance levels typically range from 3% to 5% STH.

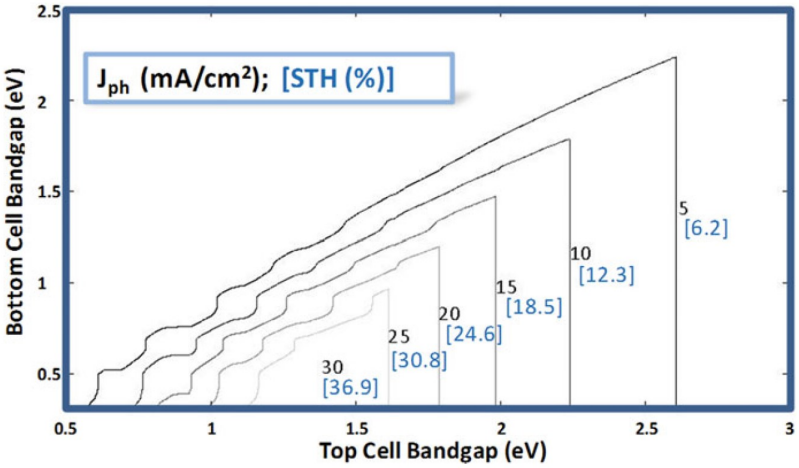

Figure 3.5: Maximum achievable photocurrent densities in tandem semiconductor devices as a function of top and bottom cell bandgaps based on theoretical optical absorption limits. Included in brackets are the corresponding PEC STH efficiencies achievable in devices capable of water splitting [9].

Similar to single-junction PV or PEC devices, multijunction configurations have efficiency limits determined by optical absorption constraints.

Fig. 3.5 illustrates the maximum photocurrent and the corresponding STH levels in PEC devices, depending on the bandgaps of both the top and bottom junctions. The assumptions made in deriving this graph are as follows:

1. The top cell absorbs all photons with energies higher than its bandgap.
2. The bottom cell is exposed to the filtered light transmitted through the top cell and absorbs all remaining photons with energies exceeding its bandgap.
3. Each absorbed photon generates an electron-hole pair, which contributes to the photocurrent.
4. The total photocurrent of the stack is determined by the smaller of the two photocurrents produced by each cell.
5. For PEC cells, the STH efficiencies (indicated in brackets on the plot) are calculated using Eq. 2.30.

These only apply to systems with sufficient photopotentials for water splitting.

Despite the inherent reduction in photocurrent due to the tandem arrangement, a wide range of bandgap combinations can yield photocurrents high enough to achieve STH conversion efficiencies exceeding 10%. The useable potential of a single cell typically ranges from 50 to 70% of the semiconductor bandgap, with the upper limit of 70% achievable only in the highest quality materials. Additionally, the photopotential of the tandem device must exceed the water-splitting potential, along with the required overpotentials, which typically amounts to around 1.6 V. Consequently, the combined bandgap of the two-component semiconductor materials

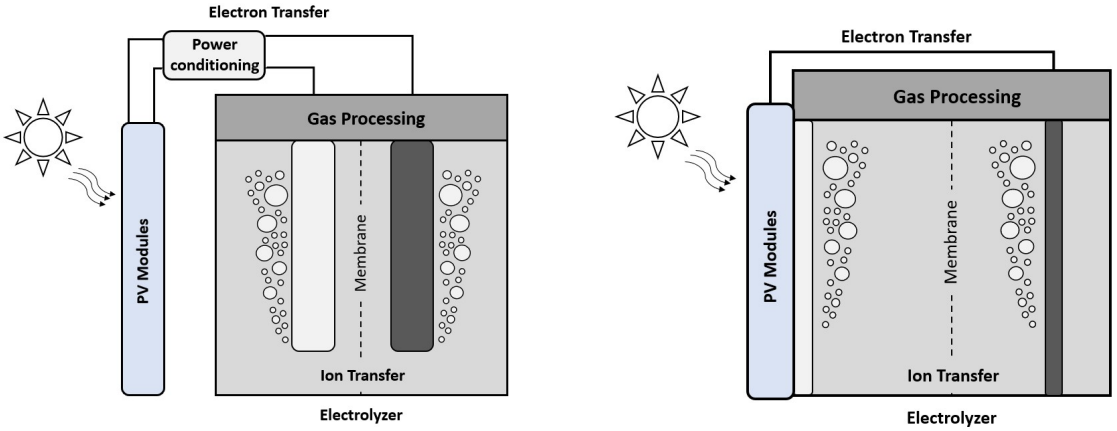

Figure 3.6: Interconnected PV–electrolyzer system with power conditioning unit (*left*); area-matched integrated PV–electrolyzer system (*right*) [9].

should fall within the range of 2.3 to 3.2 eV.
The thermodynamic limit for tandem devices under ideal conditions, including thermalization losses but no overpotential losses, has been calculated to be approximately 40% STH. This aligns with the optical limits depicted in Fig. 3.5 and represents a significant improvement compared to the 30% STH limit observed in single-junction devices. Furthermore, advanced multi-exciton device schemes that mitigate part of the thermalization losses can push the theoretical tandem limit even higher to 46% STH [37].
When considering optical, thermalization, and overpotential losses in tandem devices utilizing high-quality III-V semiconductors [33], the STH efficiency limits are slightly lower than the optical limits. However, they still exceed 25% within a limited range of top and bottom cell bandgaps. The high-quality factor of the modeled semiconductors contributes to maintaining high levels of performance. Lower-quality thin-film materials would generally experience larger efficiency reductions. Nevertheless, there should be sufficient margin to achieve STH conversion efficiencies above 10% in thin film tandem devices under certain circumstances [38].

3.3 PV - Electrolysis Systems

Several different multijunction device schemes incorporating a combination of PEC cells, or a combination of PEC and PV cells have been explored in attempts to enhance solar hydrogen production via water splitting [39]. Researchers have explored three main categories of PEC plant configurations: combined PV-electrolysis systems; photoelectrode-based systems; and photocatalyst-based slurry systems.

The primary device being developed for solar water splitting is the "PV-Electrolysis" con-

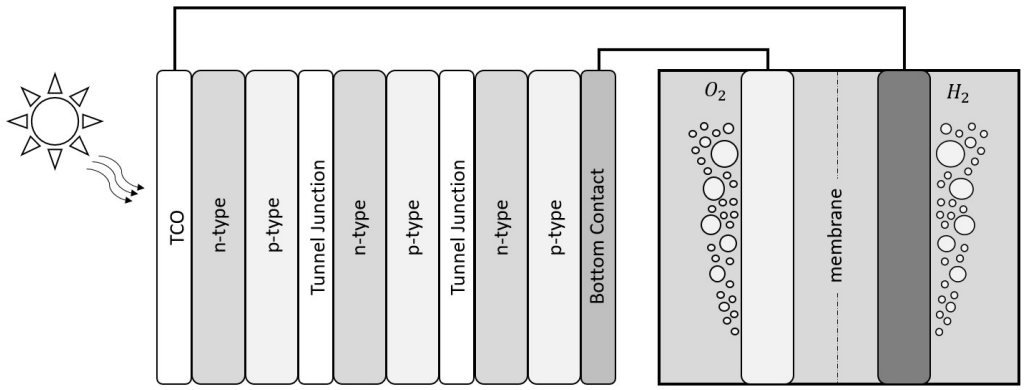

Figure 3.7: Triple-junction PV cell coupled to an electrolyzer system [9].

figuration, as depicted in Fig. 3.6 (*left*). This setup involves coupling PV panels with separate commercial electrolyzer units, such as alkaline or PEM electrolyzers. Appropriate power-conditioning equipment is then utilized to load-match the processes efficiently. An alternative variation of this approach is the integrated PV-electrolyzer unit, shown in Fig. 3.6 (*right*). Here, PV cells with adequate useable photopotential for direct electrolysis are combined with fully integrated electrolyzer systems. In this case, since the PV output of the multijunction cell is designed to have direct compatibility with electrolysis, no power conditioning units are required, reducing transmission losses.
Typically, in the PV-electrolysis category, the photoactive components in the "photoelectrode-based systems" configuration are not submerged in the solution. Fig. 3.7 illustrates a triple-junction PV cell coupled to an electrolyzer system. The usable potential generated by the triple-junction is capable of simultaneously driving photoholes at the electrolyzer anode surface and photoelectrons at the electrolyzer cathode surface. The standard design strategies of current and lattice matching are necessary for the PV semiconductor stack. Furthermore, the PV output voltage and current must be adjusted to match the optimal operating conditions of the electrolyzer system. The electrolysis process can be independently optimized with suitable electrodes and catalysts. Since there are no PEC cells in the device stack, concerns about semiconductor durability in the solution are avoided. Although some auxiliary system losses including the lateral collection of current from the PV system and transmission of electrons through external wiring are inevitable, efforts can be made to minimize them. However, cost remains a persistent challenge in this approach.

3.3.1 Monolithically Integrated PV - PEC Device

"Wireless" monolithically integrated photoelectrochemical water-splitting devices were reported in 1977 using platinized $SrTiO_3$ [40]. However, its bandgap, E_g, and the ones of related metal oxides are too large to allow for highly efficient use of the solar spectrum [41]. On the other

hand, smaller band gap materials are generally unstable to photocorrosion in aqueous solutions and need to be protected, generally with coatings of transparent, conductive oxides (TCO), to provide stable operation [42]. Fluorine-doped tin oxide (FTO) is one of the most popular TCOs, whose low resistivity strongly depends on the high carrier concentration produced by oxygen vacancy and the quantity of substitution fluorine.
TCO-coated amorphous hydrogenated Si (a-Si:H) triple junction structures have been widely explored in monolithically integrated water-splitting systems in which the photoelectrode, protection layers, and electrocatalytic species share a common optical path [43]. Use of a-Si:H triple junctions in monolithically integrated structures protected by TCOs, in conjunction with either Pt or with earth-abundant electrocatalysts for the hydrogen-evolution reaction (HER) and oxygen-evolution reaction (OER), have yielded solar-to-hydrogen efficiencies of up to 5% [44]. In monolithically integrated solar-fuel devices, tandem structures can provide significantly higher efficiencies than triple junctions [45]. For example, a photovoltaic-biased photoelectrosynthetic device based on a III–V tandem structure has exhibited 12.4% solar-to-hydrogen conversion efficiency, η_{STH}, under concentrated solar illumination. However, III–V semiconductors photocorrode both under HER and OER operating conditions [46], and therefore require protection to be utilized in such applications [6].
In general, integrating "buried" photovoltaic junctions can provide the needed photovoltage and overpotentials for bias-free water photoelectrolysis. Among the diverse challenges, the lack of certain highly efficient catalyst elements, such as Ir and Ru, makes the photoelectrolysis of water a difficult task. Transition-metal-based (oxy)hydroxides (TMOs) have proven so far to be the most active OER electrocatalysts [18]. They meet the requirements in terms of catalytic activity and stability, structural durability, elemental abundance, and low production cost for the practical operation of commercial water electrolysis. Among TMOs, oxide perovskites (ABO_3) have shown high efficiency and stability for the OER in alkaline water electrolysis. The increasing interest in oxide perovskites stems from their chemical stability, as well as their structural, compositional, and electronic versatility.

3.4 Upscaling Challenges and Membranes

Although the requirement to develop the technology towards large-scale applications, research is almost exclusively focused on laboratory experiments. Comparatively little effort has been devoted to the design and realization of large area or at least scalable devices. Taking the recent progress of photovoltaic energy conversion as a paradigm for successful implementation of a renewable energy technology, it becomes clear that in the end cost-effectiveness becomes as much a question of clever device design and process engineering as a question of optimized components. This especially applies to water-splitting devices, which require both a proper management of photons and electrons in the photovoltaic part and of the ions in the electrochemical part. Moreover, many trade-offs between optimizing different components show up only with completed, fully integrated devices.

Several modeling and simulation papers have indeed investigated device scale-up, but most experimental studies thus far have only demonstrated devices with active areas less than 1 cm^2. Notable exceptions are the work of Turan *et al.*, who reported a 64 cm^2 PV-EC module (consisting of identical 13 base units) based on Si heterojunction solar cells and nickel catalysts with 3.9% STH efficiency [47], and the impressive 1.6 m^2 PEC-PV system reported by the ARTIPHYCTION consortium. The latter is based on combining 100 PEC cells with a 64 cm^2 $BiVO_4$- based photoanodes window (it is not a true tandem system) [48]. Although no standalone device was demonstrated, Lu *et al.* very recently reported the fabrication of cobalt-doped $BiVO_4$ (Co:$BiVO_4$) photoanodes with an area of up to 300 cm^2 [49]. They showed that simply increasing the electrode area decreases the photocurrent by a factor of ~ 5.

For larger area PEC–PV systems, however, factors like electrode and electrolyte conductivity, photoelectrode uniformity, pH gradient, and light scattering caused by gas bubbles may dominate the overall device performance. Therefore, to fully achieve the ambitious goals of STH efficiency (>10%) and stability of more than 10 years, more engineering efforts are still necessary to improve the photoelectrolyser reactor design, to ameliorate its fluid dynamics, as well as to further optimize the photo-electroactive materials to achieve their efficient scale-up.

Another issue to address while designing a PEC cell is the mixture of the produced gasses. To avoid mixing the produced fuel (hydrogen or carbon-based products) with oxygen gas, ion exchange membranes are applied to separate the anodic and cathodic electrolytes in proposed solar fuel designs, such as proton exchange membranes (PEMs), bipolar membranes (BPMs), and anion exchange membranes (AEMs).

PEMs can be used in solar fuel devices to allow the transport of H^+ from the anode to the cathode. The most commonly used proton exchange membrane is Nafion®, known for its high conductivity, high chemical stability, and optical transparency. Nevertheless, the price of these membranes is high, which is an issue because the low current density requires a large area.

To increase the compatibility of photoanodes and photocathodes, a bipolar membrane (BPM) can be used to separate the anodic and cathodic electrolytes. A bipolar membrane dissociates water into H^+ and OH^- due to the two-layered ion membrane structure, which allows for maintaining a different pH on either side of the membrane. Compared to the other ion exchange membranes, the use of such membrane provides the additional advantage of using different (stable) pH at either electrode.

As an alternative to the proton exchange membranes, AEMs are proposed for solar fuel devices as well, since only allow the transport of OH^- anions. This is particularly attractive for alkaline electrolytes, while for near-neutral solutions, anion species other than OH^- are also transported, which creates additional voltage loss after multiple hours of operation. In addition, they suffer from limited chemical stability in strongly alkaline environments, lower conductivity, and limited selectivity leading to cation crossover instead of OH^- transport [50].

Chapter 4

Experimental

Two main experimental configurations can be distinguished for photocurrent measurements: one for performance and stability measurements under high-intensity white light, and the other for measuring wavelength-dependent properties using a (low-intensity) monochromatic light source. The ultimate test for any PEC device or individual photoelectrode is its performance under solar irradiation. Most PEC research laboratories are equipped with a solar simulator in order to access sunlight of constant intensity. Detailed insights into the factors that limit the performance of a photoelectrochemical device or photoelectrode can be obtained by measuring the photocurrent as a function of wavelength.
In this chapter, the instruments, the experimental setup, the materials, and the procedure used to perform the simulated sunlight measurements on the prepared device will be discussed. The goal was to collect data, in particular the estimation of the produced H_2, based on the water displacement method from a PV-PEC device using a solar simulator as an illuminating source. The setup used was composed by:

- Solar Simulator
- Pumping system
- PV-PEC device
- Additional components

4.1 Instrumentation

4.1.1 The Solar Simulator

The main figure of merit for a solar water-splitting device is its performance under real sunlight. However, even real sunlight does not have the same intensity and spectral distribution

everywhere on Earth. To facilitate meaningful comparisons of device performances, the performance characteristics are usually quoted for the so-called AM1.5G conditions. This stands for "air mass 1.5 global," and refers to the spectral distribution and intensity of sunlight on a 37° south-facing tilted surface after it has traveled through 1.5 times the thickness of the earth's atmosphere. The latter corresponds to a solar zenith angle of 48.19°. The AM1.5G spectrum includes both the direct and the diffuse contributions of the incident sunlight and has a total integrated intensity of 1.000 W/m^2.
Since real AM1.5G sunlight is not readily available at all times and at all locations, solar simulators are used. The NEWPORT Corporation's *Oriel*® Sol3A™ Class AAA Solar Simulator was used for the simulated sunlight measurements. These large area sources use a xenon lamp and a proprietary filter that efficiently and reliably meets Class AAA performance parameters without compromising the 1 SUN output power. The whole chassis was placed obliquely with respect to the solar beam with an angle of 30°.
To obtain 1 SUN output power, the solar simulator was calibrated with a calibration cell placed on an aluminum support in such a way that the middle of it was 86 cm underneath the lamp. A 1.001-1.005 range of Sun values was obtained for 10 minutes, with a homogeneous diffusion. Switching off the lamp gave a 0.013 output due to the laboratory's lights, therefore approximately 99% of the light reaching the cell is coming from the simulator.

4.1.2 The Pumping System

To collect the produced gases and refill the electrolyte chamber, a peristaltic pump was connected to the PEC device (Fig. 4.1 *right*). This type of pump, commonly known as a roller pump, is a positive displacement pump used for various fluids. The fluid is contained in a flexible tube fitted inside a circular pump casing. Most peristaltic pumps work through rotary motion, in our case a Golander BT100S 2xYZ15, with two pump heads was used.
In such a way, the part of the tube under compression is closed, forcing the fluid to move through the tube. Additionally, as the tube opens to its natural state after the rollers pass, more fluid is drawn into the tube. This process is called peristalsis and is used in many biological systems such as the gastrointestinal tract. A reservoir is connected to the chassis through an inlet and an outlet pipe, as depicted in Fig. 4.9 (*left*). These two pipes are connected to the two heads of the peristaltic pump. The setup allows the removal of bubbles from the chassis and simultaneously recycling the electrolyte while collecting hydrogen and oxygen.
This type of pump was chosen due to several advantages: it is extremely effective when pumping fluids that contain trapped gases, as in this case; there is no contamination since the only part of the pump in contact with the fluid is the interior of the tube. Furthermore, it requires low maintenance and it is easy to clean; the lack of valves, seals, and glands makes this type of pump a lot cheaper.
Nevertheless, the flexible tubing, made of Tygon S3-E-3603 will tend to degrade with time and will require periodic replacement in the future.

Figure 4.1: Visualization of the solar simulator during the calibration test (*left*). The cell is put 86 cm away from the lamp to obtain 1 SUN output power. Visualization of the pumping system (*right*). The two head pumps are connected to the inlets and outlets of the device.

4.2 The Starting Device

In the work of Zhu *et al.*, a PV-PEC device was built with BGLC587 ($x = 0.5$ $y = 0.2$) deposited on F-doped SnO_2-coated glass (FTO) as the OER electrocatalyst, and a NiMo film deposited on Ti foil as the HER electrocatalyst. A schematic of the device is shown in Fig. 4.2 (*left*).
First, BGLC587 was deposited on the FTO by pulsed laser deposition (PLD). Then, a mini-PV module was prepared by four, series-connected solar cells (1×1.2 cm) with shingled interconnection, cut from commercial p-type monocrystalline silicon Passivated Emitter and Rear Cells (PERC) with a conversion efficiency of 20.5%. The interconnection overlap between the solar cells is 2 mm, resulting in an illumination area of 4 cm^2. Their configuration is shown in Fig. 4.2 (*right*). The mini-PV module was laminated with standard Ethylene Vinyl Acetate (EVA) as the encapsulant, cathode substrate (Ti foil) at the backside, and the BGLC587-coated FTO as the front side. After lamination, the NiMo HER catalyst was electrodeposited on the Ti foil

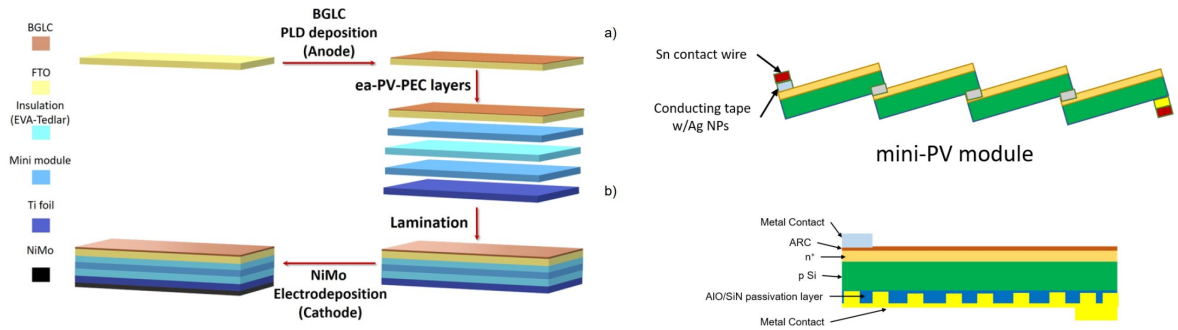

Figure 4.2: Schematic presentation of the assembly of the ea-PV-PEC device. For simplicity, not all the layers are represented. The illuminated area matched the electrode area of 4 cm^2 (*left*). The solar cells were laser cut in 1 × 1.2 cm and an overlap of 0.2 × 1 cm was utilized to fasten them together with Ag NPs filled conducting tape. In the same way, Sn contact wires were also attached (a). Schematic cross-section of the individual Si solar cells used in the mini-PV module (b) (*right*). ARC: Anti Reflection Coating [5].

of the whole assembly (back side of the layered structure). Fig.4.3 shows the operating condition of the whole device. As in layered oxides, the vacant lattice oxygen sites at the surface participate in the OER, labeled as the Lattice oxygen Oxidation Mechanism (LOM), leading to an amorphization of the surface itself. Increasing oxygen vacancy concentration increases both oxide ion conductivity and OER by facilitating more surface reaction sites (vacancies). As surface amorphization is only initial and eventually comes to equilibrium with the crystalline bulk, exchange rates under current must be equal, therefore the Adsorbate Evolution Mechanism (AEM) or the equilibrated LOM is assumed to be dominant, and the current is all faradaic.

After operations, BGLC587 also loses the A-site ordering but maintains the crystalline perovskite structure. Post-operation analysis highlights a decrease in Barium content and also shows the expected formation of a thin (approximately 5-6 nm after 48 hours of operation) amorphous layer, which has been observed in several other perovskite materials operating in alkaline electrolytes [51]. Nevertheless, the performance is not affected by these events. Moreover, the Ba loss is compensated by the formation of electron holes, which further promote the OER.

The BGLC587-coated glass shows over 70% of the transmittance in the visible region, where the EQE has an excellent response. The operation of the ea-PV-PEC device under solar-simulated light was investigated for more than 70 h, showing that the ea-PV-PEC device under bias-free, wireless operation exhibits photocurrent densities ranging from 5.0 to 5.4 mA/cm^2 leading to a maximum STH of 6.6%. Furthermore, the experiment was performed also outside for realistic operating conditions, yielding, under 1 sun intensity, an STH of approximately 5%, consistent with the indoor performance values obtained indoors for longer times (more than 70 hours). The photocurrent density fluctuates significantly due to the passing of clouds however,

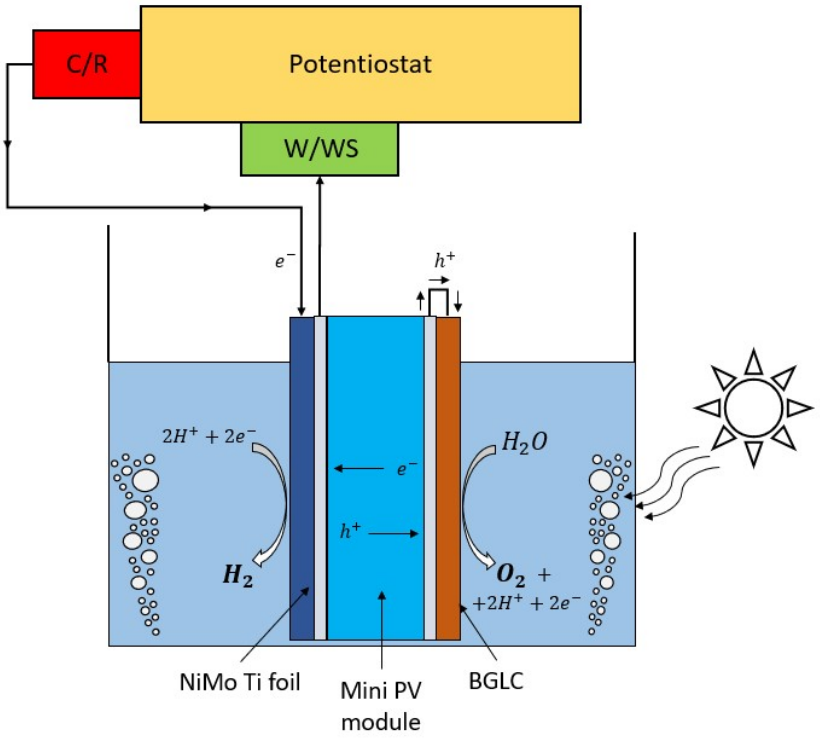

Figure 4.3: ea-PV-PEC device configuration with a potentiostat connected in series. The p-terminal of the minimodule is short-circuited by the Ag ink with the anode (BGLC on FTO) and insulated by epoxy. The n-terminal of the minimodule is connected with the working/working sense (W/WS) lead of the potentiostat. In contrast, the uncoated part of the Ti foil is connected to the counter/reference (C/R) lead of the potentiostat. The flow of the electrons and holes is also represented. In this way, the presence of contacts in the electrolysis solution is avoided, but the evaporating electrolyte needed compensation [5].

the STH efficiency remains between 4% and 5%.
The amorphization of the BGLC surface during operation in alkaline conditions is not seen to degrade the performance over time. This indicates that the surface reaction is well-catalyzed by the AEM even when Co oxide is suspended in an amorphous matrix of Ba, Gd, and La oxides or hydroxides. However, due to high partial oxide ion conductivity and since the total BGLC layer is only 30 nm thick, the complete amorphization after 71 hours, leads to irreversible performance degradation, emphasizing the significance of crystalline BGLC on cell performance [5].

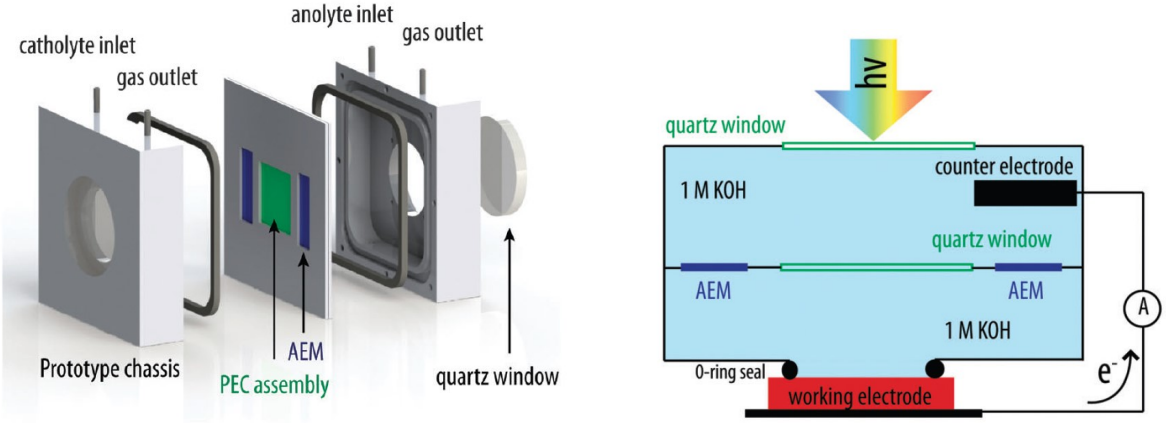

Figure 4.4: Schematic illustration of the cell prototype from Verlage *et al.* [6]. A fully monolithically integrated intrinsically safe, solar-hydrogen system prototype (*left*). A schematic illustration of the two-electrode cell configuration, in which the photoanode and the cathode were separated by an anion exchange membrane (*right*).

4.3 Design of the Inner Chassis

The photoelectrochemical cell investigated was a scale-up of a previous PV-E device where $Ba_{1-x}Gd_{1-y}La_{x+y}Co_2O_{6-\delta}$ (BGLC) is combined with a NiMo cathode [5]. The whole purpose of the project was to increase the dimensions of this device and understand the consequences in terms of efficiency, stability, and catalyst activity. The PV-PEC device was inserted in a larger chassis than used in the literature. The chassis contained the electrolyte and used a pumping system that allowed its recycling and avoided the formation of bubbles that could jeopardize the light absorption process. Several designs were evaluated during the thesis, and a similar configuration of the work from Verlage *et al.* was finally chosen [6], Fig. 4.4. In the design of Verlage, a PV-biased electrosynthetic cell consisting of a $GaAs/GaInP_2/TiO_2/Ni$ photoanode was connected to a Ni-Mo coated counter electrode allowing unassisted solar-driven water-splitting for 80 hours of continuous operation at 1 Sun illumination in 1.0 M $KOH(aq)$, with $\eta_{STH} = 10.5\%$. The photoanode and the cathode were separated by an anion exchange membranes.

Several problems occurred, like the formation of bubbles due to the O-rings' compartments and the corrosion due to minimal pathways in the TiO_2 film. Nevertheless, this configuration was chosen due to its similarities with our project: the monolithically integrated device, the use of the membranes, and the wireless setup are crucial components of the up-scaling challenge.

Major modifications are needed, though, to properly create an up-scaled device: an additional membrane is placed due to the greater volume of the electrolyte, and the inner unit in the prototype cannot be flat due to the different thicknesses of the cell and the membranes. A box-shaped design is chosen to accommodate the different parts. This led to additional O-rings, positioned

around the three AEMs. Moreover, the need to recycle the electrolyte leads to a substantial change in the prototype: along with the gas outlets, electrolyte inlets are placed at the bottom of the chassis to allow the pumping system to refill the whole device with the KOH solution.

4.3.1 The Final Photovoltaic - Electrolyte Cell

The project aimed to increase the dimensions of the previous device up to a 10 cm^2 PV-E cell. A 5 × 5 cm model was built in the same way as the starting device. Onto the 25 cm^2 titanium foil, Ni-Mo was partially electrodeposited in a 2 × 5 cm region. As for the PV panels, they were stacked in a 3 × 3.5 cm configuration, obtaining an active surface area of 10.2 cm^2. To perform the simulated sunlight measurements, a container was built to accommodate the PV-E device.
The design process comprehended first, the study of the mechanical properties evaluating the initial chassis with the use of a 3D printer: the object was made with the FreeCAD 0.20 software and connected to the printer (Pruse i3 Mk3/Mk3s) with the UltiMaker Cura 5.3.0. Several printed designs were analyzed before choosing the proper one. The options differed on the width of the plates, the number of membranes, the width of the O-rings, or the size of the whole chassis. Eventually, the final design was selected and built in the laboratory.
The inner box is made of two Teflon plates (120 × 120 × 16 cm), as can be seen in Fig. 4.5 (*left*), in such a way that the PV-E model is sandwiched in between by pressurizing the plates with stainless steel screws. The material was chosen due to the electrolyte's alkaline nature and Teflon's passive nature in these solutions. Additionally, due to its weakness to intense stresses, the thickness of the plates was also increased up to 8 mm each, to avoid the bending of the material in the sandwich configuration. To properly pressurize the inner chassis, a 316L stainless steel (that shows excellent compatibility with Potassium Hydroxide [52]) skeleton in an *x* pattern is applied in both plates (Fig. 4.5 *right*).

Next, a larger container is constructed, following a similar design approach. Two plates are pressed together to create space for both the electrolyte and the inner box (Fig. 4.6). The electrolyte, potassium hydroxide (KOH), is poured into the chassis, filling its 214 mL volume. To enable the photoelectrocatalysis process, a quartz window is incorporated. Several O-rings (2 mm diameter) are placed to insulate the PEC from the electrolyte, in such a way that only the front and back parts of the device come into contact with it.
Three Anion Exchange Membranes are needed to safely separate the different products (H_2 and O_2 gases) without creating hazardous mixtures, therefore preventing the diffusive and convective crossover of products between the cathode and anode chamber.

4.3.2 Additional Components

The inner cell, which contains the PV-PEC device and the three membranes, is inserted in a larger container filled with the electrolyte. The chassis design was developed with the FreeCAD 0.20 software and printed (using the 3D printer Pruse i3 Mk3/Mk3s) with the UltiMaker Cura

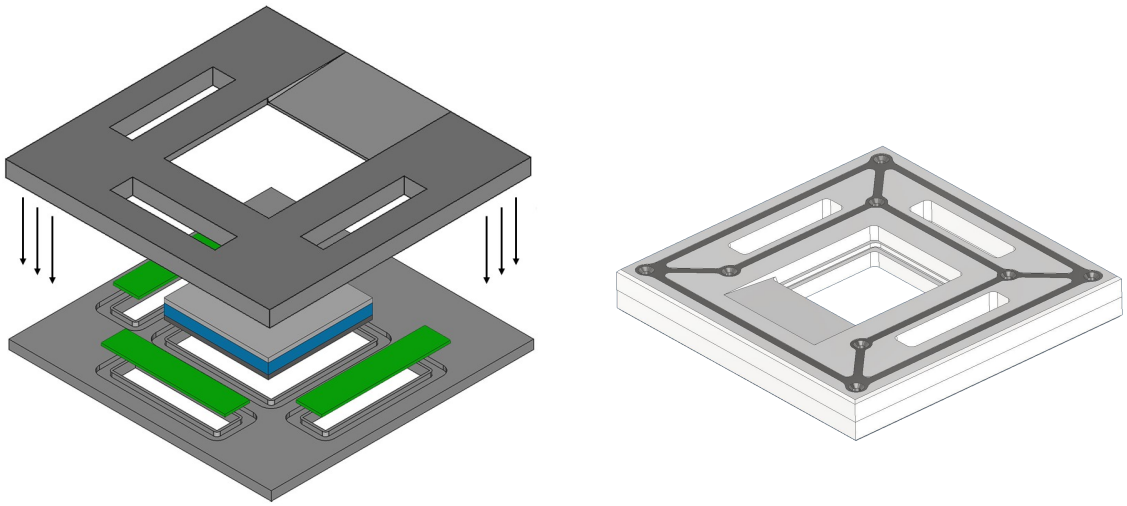

Figure 4.5: Schematic illustration of the inner cell prototype. The three AEMs (*green*) are placed all around the PV (*blue*) - PEC device (anode and cathode in *light* and *dark gray*, respectively). An angular narrowing can be seen on the top plate, in contact with the electrolyte, to provide a pathway thus avoiding the concentration of bubbles during operations (*left*). The pressurized container, with an *x* pattern stainless steel 316L skeleton (*right*).

5.3.0 in order to test the mechanical stability and the goodness of the thicknesses of the device. The final design is shown in Fig. 4.6 (*left*), where the chassis is constructed in such a way that the inner cell can be sandwiched between two compartments (anolyte and catholyte) sealed with O-rings. A quartz window is present to allow photoelectrocatalysis. The pumping system is connected to both compartments: three holes at the bottom allow the recycling of the electrolyte, and the one on top collects hydrogen and oxygen.

A round quartz window is then applied to the square hole on the top side. Support is constructed to properly seal the electrolyte with an O-ring and linked to the screws of the outer chassis, as depicted in Fig. 4.6 (*left*).
A glass reservoir is filled with 500 mL of 1 M KOH and then connected to the tubes. Two glass separators Fig. 4.7 (*left*) have been applied to the two outlet tubes, in such a way that the bottom entrance is connected to the second head pump and the top one collects the gases into the water tank. In these three-gate 200 mL cylinders (one inlet from the PV-E device and two outlets), the electrolyte is separated from both hydrogen and oxygen, as can be also seen in the experimental setup (Fig. 4.9 *B-02, B-03*). The tubes' connections are made with Swagelok stainless steel 316 union crosses (one inlet and three outlets), as shown in Fig. 4.7 (*right*).

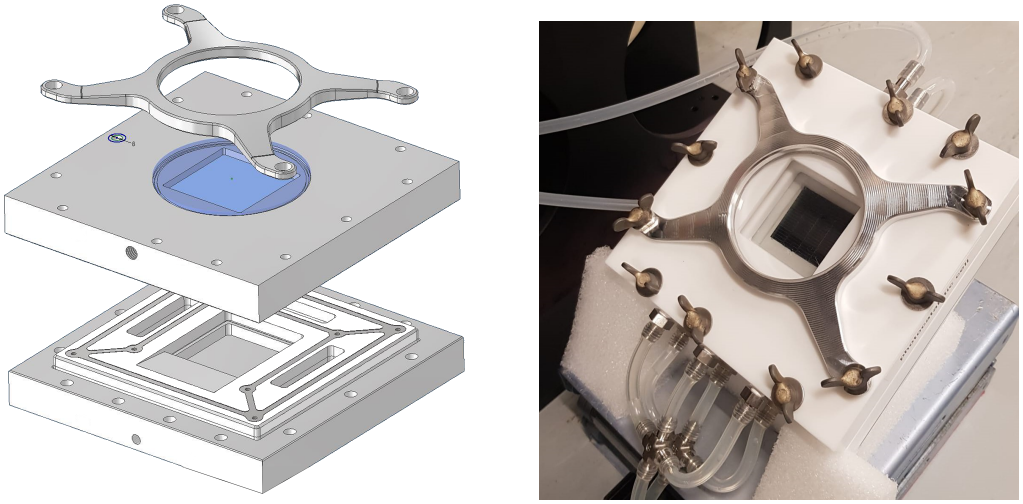

Figure 4.6: Prototype of the outer chassis. The inner cell is sandwiched in the larger container with two compartments. The eight inlets (three at the rear and one at the front for each compartment), and the quartz window along with its support, are shown. Picture of the final assembled device (*right*).

4.4 Material Characterization

As of today, iridium/ruthenium oxides are regarded as benchmark electrocatalysts for OER due to their excellent catalytic activity in both acidic and alkaline environments [53]. The Ir-/Ru-oxides typically exhibit low overpotentials and low Tafel slopes. However, it is observed that the activity of these may vary depending on electrolyte concentration, morphology, and from different reported studies.
Even though IrO_2 and RuO_2 show favorable activity towards the OER, their high cost and limited abundance compared to i.e. transition metals have hindered the large-scale deployment of these in industry. Another reported drawback of these noble metal oxides is the low stability in acidic and alkaline environments during OER, caused by the oxidation of IrO_2 and RuO_2 to IrO_3 and RuO_4 which may dissolve into the electrolyte [54, 55]. In general, dissolution is more prominent in alkaline solutions, in which IrO_2 is considered the most stable and RuO_2 the most active. For these reasons, an increasingly popular choice as electrocatalysts for the OER during the last decades, are those exhibiting the perovskite structure. The interest in these comes from their highly tuneable (electro-)chemical and physicochemical properties originating from their great versatility in elemental composition.
As for the Hydrogen Evolution Reaction, transition metal alloys have been extensively studied as hydrogen electrodes in water electrolysis, and electrolytic co-deposition is a commonly employed technique for their electrode fabrication.

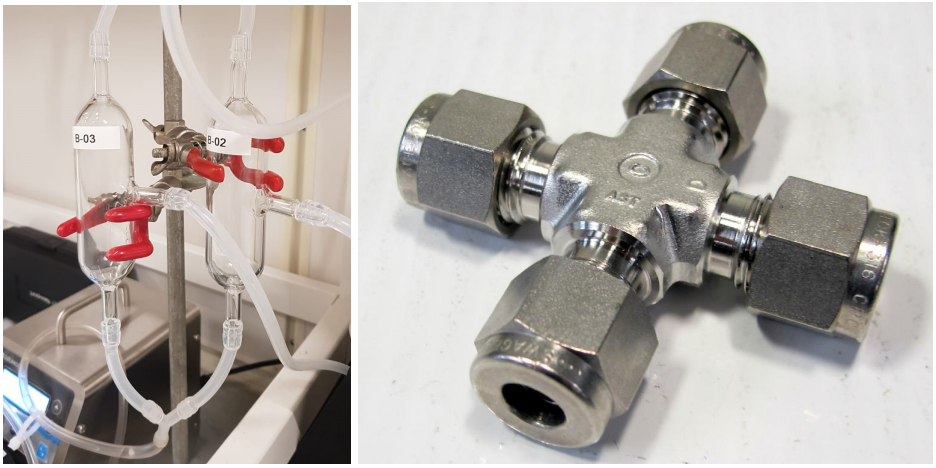

Figure 4.7: Glass separator used for the collection of gasses (*left*). Swagelok stainless steel 316 union cross used for the tube connections (*right*).

4.4.1 Nickel-Molybdenum Electrodeposition

In his investigation of hydrogen electrodes based on the Brewer-Engel theory, Jakšić reported that whenever metals of the left half of the transition series in the periodic table with empty or less-filled d-orbitals are alloyed with metals of the right half of the series with more filled d-bands, a maximum in bond strength and stability of the intermetallic alloy phases is expected [56]. This phenomenon demonstrates a well-pronounced synergism effect in electrocatalysis. To avoid the use of noble metals as catalysts, suitable transition metals from the right half of the series include iron, cobalt, and nickel, which are part of the 3d series. From left-lying transition metals, the preferable elements are those with extended d-orbitals which provide less distortion and improved d-orbital overlap, such as tungsten, molybdenum, lanthanum, hafnium, zirconium, and others [57]. In this specific case, a Nickel-Molybdenum electrode was electrodeposited for the HER in a 30% weight percent (w/o) KOH alkaline water-electrolyte at a temperature of 25 $°C$.
To initiate the cathode preparation process, the LAQUA D-71 pH meter was first calibrated to ensure accurate pH measurements of the solutions. The desired bath composition and deposit conditions for Ni-Mo are achieved by adding ammonia (NH_3) to a slightly acidic solution, resulting in a pH of 10.5. Subsequently, a two-electrode system is employed to perform a test deposition, initially on a Titanium foil. A 2×5 cm active surface area is considered when submerging the Ti foil in the solution along with a Nickel foam and a magnetic stirrer for electrodeposition. Once the viability of the process was demonstrated, the PV-PEC cell was cleaned with isopropanol and then partially submerged in the solution, always with a 10 cm^2 active surface area. A current step of -200 mA (the negative sign indicates Nickel deposition on the cathode side) is applied for 15 minutes to drive electrodeposition.

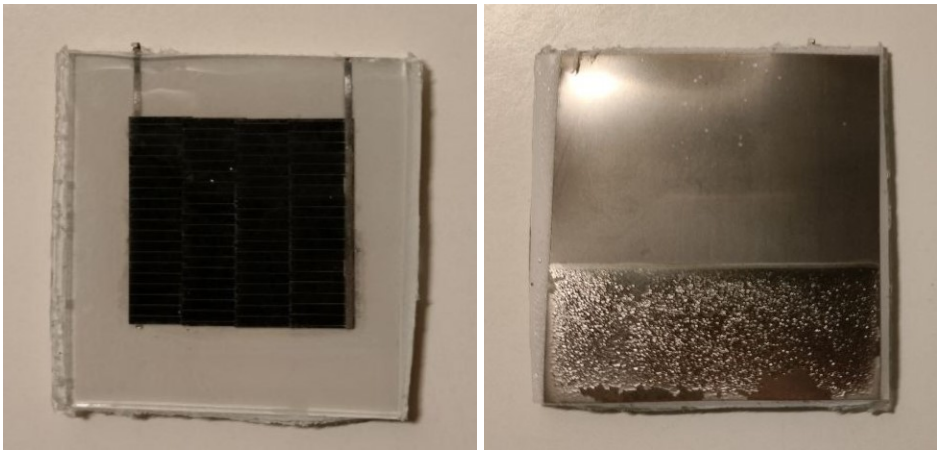

Figure 4.8: Anode (*left*) and cathode (*right*) of the PV-E cell. The anode is made of an FTO over a 3x3.5 PV grid, and BGLCF70 drop-casted on top (dried black ink). The electrodeposition of NiMo on the Ti foil can also be seen on the cathode (lower part).

4.4.2 Catalyst Material: BGLC

Recently, perovskite cobaltites with the general formula $Ba_{1-x}Gd_{0.8-y}La_{0.2+x+y}Co_2O_{6-\delta}$ (BGLC) were found to be stable and efficient anode materials for proton ceramic electrolyzers (PCEs) operating at temperatures around 600 $°C$ [58]. Building on this finding, further investigations were conducted on BGLC as electrocatalysts for the oxygen evolution reaction (OER) at room temperature under alkaline conditions. These revealed several stoichiometries showing promising activities, with the compound $Ba_{0.5}Gd_{0.8}La_{0.7}Co_2O_{6-\delta}$ (BGLC587) exhibiting the highest activity and stability [59, 5]. However, one of the aims of this study is to reduce the cobalt content in BGLC587 by substituting it with more environmentally friendly transition metals such as iron (Fe) and nickel (Ni).
For this purpose, our main hypothesis is that elements such as Fe and Ni, when substituted into the B-site of BGLC587, can enhance its OER performance. We support this hypothesis by referring to results from the literature, in which both Fe- and Ni-based electrocatalysts have demonstrated good OER activity, as well as stability [60, 61, 62]. One such material containing iron is $Ba_{0.5}Sr_{0.5}Co_{0.8}Fe_{0.2}O_{3-\delta}$ (BSCF82), which exhibits exceptional specific activity and is considered the benchmark perovskite oxide electrocatalyst for the OER [63].
In our specific case, a 300 μL $Ba_{0.5}Gd_{0.8}La_{0.7}Co_{0.6}Fe_{1.4}O_{6-\delta}$ (BGLCF70) ink was drop-casted onto the FTO substrate as a catalyst and left to dry for 30 minutes.
The final result is shown in Fig.4.8.

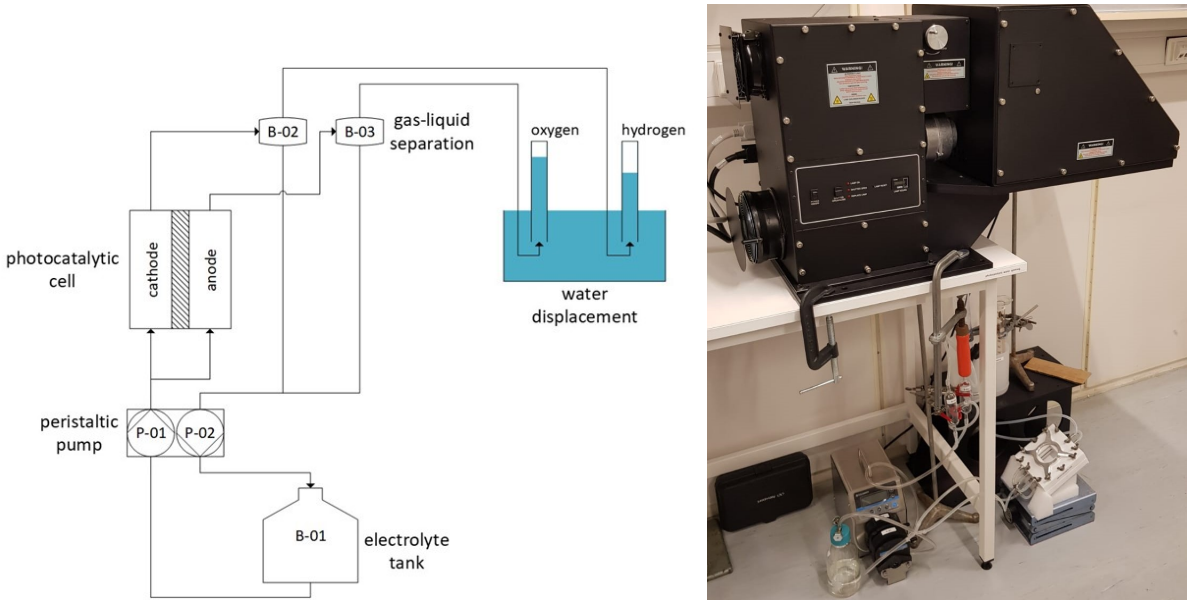

Figure 4.9: Scheme of the Experimental Setup (*left*). The reservoir is connected to the inlets of the device through a peristaltic pump (*P-01*), to refill the electrolyte. Two outlets collect both hydrogen and oxygen, where two separators split them up from the electrolyte (*B-02*, *B-03*). The second head pump drains the remaining electrolyte (*P-02*), while the two gasses are guided in two upside-down cylinders in a water displacement configuration. A picture of the setup (*right*).

4.5 Experimental Setup

To perform the experiment, the whole device is assembled as represented in Fig. 4.9. The PV-E cell is inserted in the inner container, along with the membranes. The inner container is put inside the outer chassis, and filled with 1 M KOH electrolyte. To measure the evolved gasses, the outlets from the device are connected to upside-down tubes filled with water, passing through glass separators to properly divide the gases from the electrolyte. At the same time, the inlets are linked to a Tygon S3-E-3603 tube, through stainless steel 316 union crosses in a Swagelok configuration (from the company that builds the components). The tubes are connected, passing through the peristaltic pump, to the electrolyte in the reservoir. In such a configuration it is possible to measure the rates of the evolved gasses through the water displacement method. The experimental setup is shown in Fig. 4.9.

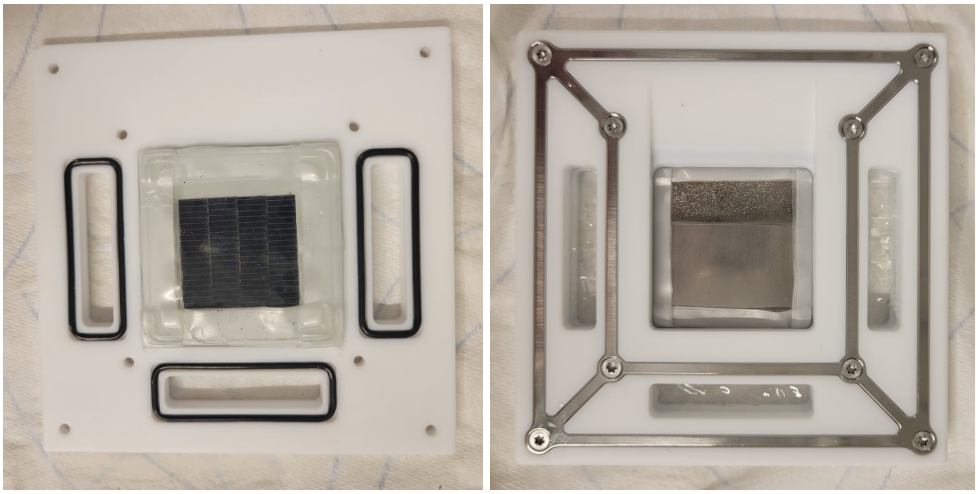

Figure 4.10: Addiction of parafilm to the device. Anode (*left*) and cathode (*right*) top view.

4.6 Acquisition Data

Before carrying out the experiment, a risk assessment paper has been prepared to properly perform the measurements. From the Zhu *et al* paper, the experiment has to be conducted within 72 hours of the illuminated response from the solar simulator, otherwise, a massive amorphization of the device would have led to the failure of the PV-PEC cell itself. For this reason, the tube was tested for more than three days in the 1 M KOH solution to see whether it would degrade. Special attention was given to the cylinders in the water tank and their volume. By assuming a maximum rate of hydrogen production of 0.4 mL/min (and subsequent 0.2 mL/min for oxygen), the dilution of the produced gases must be safe. A light-on route has been chosen for approximately 8 hours, where the hydrogen could be then safely released in the laboratory room (with a volume of more than 8000 L compared) due to its heavy dilution in the air.
After all these precautions, a leakage test was performed before the actual experiment. Water was inserted in the glass reservoir and pumped through the peristaltic pump in the device. An internal leakage was found in the inner part of the device due to a mismatch in the thicknesses between the cell and its available room in the chassis. This 1.1 mm extra space was fixed by applying some parafilm on the cell, as can be seen in Fig. 4.10. A second leakage test was performed and no spill has been detected.

At this point, the cell was allocated under the solar simulator, the glass reservoir was filled with 1 M KOH, and the pump was set to 100 rpm (revolutions per minute) to drench the device's anolyte and catholyte. The solar simulator was switched on and left to warm up for 30 minutes to reach 1 Sun due to the factory setting, before allowing it to reach the PV-PEC device with a shutter switch.

Chapter 5

Results and Discussion

5.1 Theoretical analysis

To properly evaluate the PV-E cell's performance, a brief consideration has to be made. During the experiment's time interval, two processes modify the initial conditions of the whole setup: the evaporation of water due to vapor pressure in the glass separators, and water consumption due to its chemical splitting into hydrogen and oxygen inside the cell.
Since both of these processes are temperature-dependent, the water's final volume in the electrolyte solution, and therefore its final concentration, will have different values. To safely neglect these processes, and keep considering 1 M of KOH solution, Faraday's law was used to evaluate the volumetric flow of both gasses in the water-splitting process. Assuming a maximum current in the cell of 0.4 A, the volumetric flow of hydrogen (f_{H_2}) is 0.4 mL/min, with the oxygen one (f_{O_2}) being half of this value. Applying the perfect gas law, it is possible to obtain the molar flow of both gasses for different temperatures. A realistic range of temperatures has been considered, from 278 to 343 K.
Since, from the stoichiometry of the reaction, the consumed water molar flow (f_{H_2O}) and the hydrogen molar flow are the same, it is possible to calculate the water consumed rate due to water-splitting, shown in Tab. 5.1.

Table 5.1: Theoretical values of the consumed water's flow rate due to water splitting at different temperatures. Increasing the latter leads to a lower flow rate, following the perfect gas law.

Temperature [K]	O_2 flow rate [mmol/min]	H_2 flow rate [mmol/min]	H_2O consumed rate [mmol/min]	H_2O consumed rate [μL/min]
278	0.0087	0.0175	0.0175	0.315
293	0.0083	0.0166	0.0166	0.299
313	0.0077	0.0155	0.0155	0.280
333	0.0073	0.0146	0.0146	0.263

To fully evaluate the total consumption of water, its evaporation due to vapor pressure has to be considered. Vapor pressure, or equilibrium vapor pressure, is the pressure exerted by a vapor in thermodynamic equilibrium with its condensed phases (solid or liquid) at a given temperature in a closed system, such as the glass separators.
The Antoine equation is a pragmatic mathematical expression of the relation between the vapor pressure and the temperature of pure liquid or solid substances. It is obtained by curve-fitting and is adapted to the fact that vapor pressure is usually increasing and concave as a function of temperature. It is reasonably accurate for higher temperatures however, the low ones are calculated with quite a large error. The Tetens equation works well for the 273-333 K range, with Arden Buck's relation being the most accurate for every checked value:

$$P = 0.61121 \times \exp\left(18.678 - \frac{T}{234.5}\right)\left(\frac{T}{257.14 + T}\right) \tag{5.1}$$

where P is the saturation vapor pressure in kPa, and T is the air temperature.
Though the values from Eq. 5.1 start to differ significantly for temperatures higher than 373 K, in the case of the present work it will suit perfectly.
By evaluating the ratio (r) between the saturation pressure and the atmospheric one (760 mmHg), it is possible to obtain the molar flow of the total produced gas: $f_{H_2} + f_{O_2} + (f_{H_2} + f_{O_2}) \times r$.
At this point, the water evaporated rate can be estimated, as shown in Tab. 5.2.

Table 5.2: Theoretical values of the evaporated water's flow rate at different temperatures. Increasing the latter leads to an increase in the evaporation rate, as expected from the literature.

Temperature [K]	Vapor pressure [mmHg]	Pressure ratio	Total gas rate [mmol/min]	H_2O evaporated rate [μL/min]
278	6.544	0.0086	0.0265	0.004
293	17.54	0.0231	0.0255	0.010
313	55.37	0.0728	0.0250	0.033
333	149.6	0.1968	0.0262	0.093

By adding these two contributions it is possible to evaluate how much water will be consumed during the experiment, therefore estimating the final concentration of the solution. From the Zhu *et al* paper, the amount of time before the failure of the PV-PEC device is 72 hours [5]. Both graphs in Fig.5.1 show the variation in the water volume for both a solution of 500 mL (as in our case) and of 5 L with the variation of the temperature and the subsequent concentration change.

It is safe to say then, that the consumption of water can be easily neglected during the whole experiment's time interval. Even for the extreme temperature scenario (around 333 K) the volume change is completely irrelevant, highlighting how a cooling system to mitigate the water consumption, was unnecessary.
The first experiments performed on the working setup show that the whole device worked, with

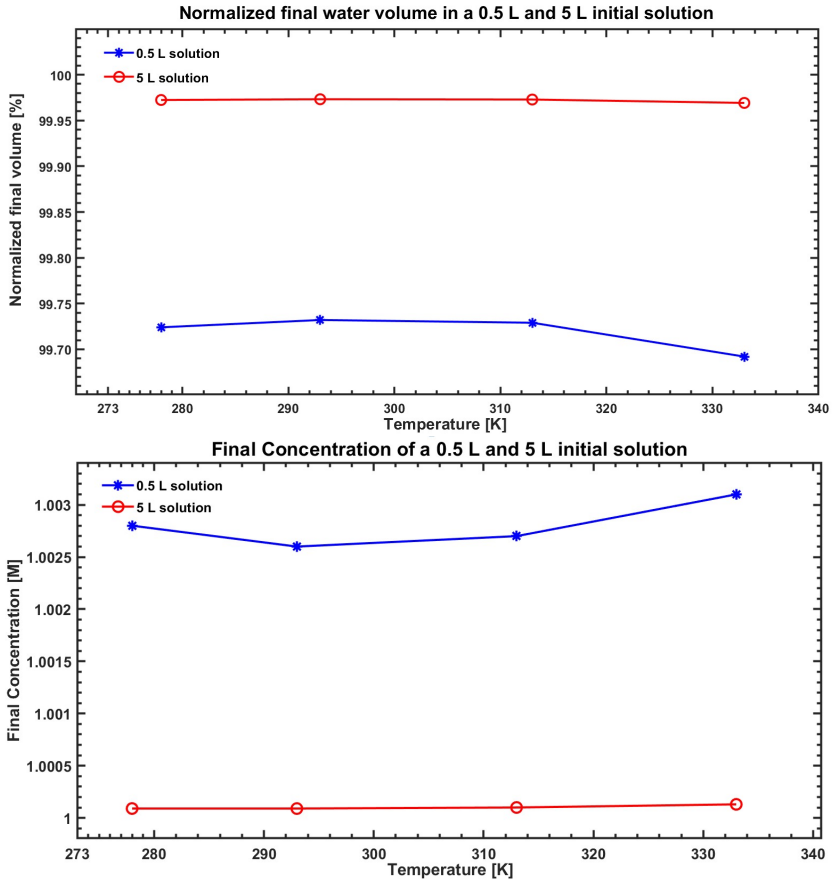

Figure 5.1: Theoretical values for normalized water volume after 72 hours (*top*). Both of the final volumes (0.5 L and 5 L solutions) are below 1%. Theoretical values for the final concentration of the solutions (*bottom*). The change in concentration is negligible for both solutions.

the water splitting occurring as proved by the formation of bubbles depicted in Fig. 5.2 (*top*). §§Some issues were highlighted during the acquisition data procedure. The production of both gasses was very low: firstly the bubbles, and therefore the produced gasses, were stuck in the device's window, and even by doubling the electrolyte's flow through the peristaltic pump, no hydrogen could be measured from the PV-E cell. After several minutes, some bubbles with a diameter of approximately 0.5 mm reached the outlet of the device but remained stuck in the tubes as dead volume, where dead signifies unmoving, stagnant, or unswept (Fig. 5.2 *bottom*). The impossibility of collecting some data is correlated with two main causes: the extremely low gas production and the presence of dead volume in the setup.

The former cause is an electrochemical concern: to increase the H_2 production, meticulous work has to be done in the electrocatalyst fabrication. It is clear that for this size of device, it is not possible to only scale up the same configurations of the smaller PV-E cell. Some further

consideration has to be made regarding the size of the electrodes. Ohmic losses in the system due to the resistance of the FTO substrate, finite conductivity of the electrolyte, and contact resistance are all cell efficiency losses, that appear by only increasing the electrode's size. Additionally, the type of semiconductor used as photovoltaic could affect the overall performance of the device. Higher efficiency, higher cost multijunction solar cells, such as the III-V materials systems capable of 20-40% PV conversion efficiency are also commercially available. Using these materials 14-28% STH could be achievable using PV-electrolysis. In today's market, however, such systems would be prohibitively expensive for any large-scale deployment.
Moreover, the complexity of the setup can be responsible for other problems. Several components can be adjusted to improve the experiment: the quartz window, the tube material, the water displacement method, the use of parafilm, and the asynchrony of the two head pumps of the peristaltic pump.
The quartz window of the cell, adjusted above the anolyte, could be smaller and better cleaned before assembling the device, to avoid the sticking of the gas bubbles that may cause light scattering before reaching the PV modules. As for the material used for the tubes (Tygon S3-E-3603) a better choice could have been polyethylene (PE) or polyvinyl chloride (PVC) but they are not compatible with this type of peristaltic pump. A new pump model should then be purchased to verify whether changing the tube material could lead to an improvement in the dead volume issue inside the tubes.
The water displacement method is a very immediate way to measure the yield of hydrogen and oxygen. Nevertheless, it adds complexity to the system since two glass separators were deployed in the setup to divide the produced gases from the electrolyte. In the case of our preliminary experiment, the production rate was too low for the bubbles to reach the water tank, therefore considering the water displacement method as the main bottleneck of the experiment is not possible. A solution to overcome this limit could be employing a flowmeter and a gas chromatograph. In such a way, purging with Argon, e.g., the tubes, and measuring the percentage of produced gasses (hydrogen and oxygen) in it with gas chromatography, would lead to a better understanding of H_2 yield.
Parafilm was employed on all four sides of the cell to accommodate it inside the inner chassis: a 1.1 mm extra space in the box-shaped area, hinders the correct sealing of the anode and cathode part from the electrolyte, causing internal leakage. Reducing this extra volume in order to avoid the parafilm addition, would lead to a less complex setup, promoting a more compact design in the cell.
Another issue, strictly connected to the low production rate of the gasses, is the fast consumption of the electrolytes inside the glass separators. This is due to a slight, but sensible asynchronism (approximately 0.5 mL/min) in the two head-pumps (the first one fills the liquid in the cell and the second one collects it from the glass separators into the reservoir) that consume, in approximately 15 minutes, the liquid inside the separators. A more precise pump would avoid this problem, allowing the glass separators to stay full for the whole experiment. Since the modification in the tube material is strictly affected by the type of compatible pump, the latter should be purchased keeping in mind this feature.

5.2 Further Investigations

This project only scratched the surface of the upscaling challenges of a PV-PEC device. Collecting data and therefore understanding the actual efficiency of the cell is nontrivial: such a scale-up reactor will need to be modified for further work to overcome all the aforementioned limitations. We suggested first facing the engineering issues, such as the tubing and pumping system and the use of adjusted measurement methods, to avoid all the artificial bottlenecks and allow the collection of the hydrogen gas.
A magnified focus should also be put on the electrocatalysts employed by performing the material characterization. This would be important to address problems related to material performance and it would facilitate interventions on the experimental setup.
At this point, several measurements can be done by changing the angle of the cell or considering longer time intervals to properly estimate what happens at the electrode surface. Tests on various scale-up device designs could be performed to compare efficiency and stability.
Other investigations could be conducted using different inks as anode catalysts. In our project, a BGLCF70 was used, but it would be of great interest to find out what happens when another ink is applied, such as different doping of the same BGLC family.

Figure 5.2: Formation of bubbles in the device. Oxygen bubbles in the anolyte (*top*). Dead volume in the Tygon tubes (*bottom*).

Chapter 6

Conclusions

To conclude, this project was aimed at increasing the size of a PV-PEC device (up-scaling procedure) to surpass the laboratory step and try to pave the way for new prototypes at the industrial stage. This aim was partially achieved: the reactor in which the upscaled cell was inserted allowed photoelectrolysis, as can be seen from the formation of bubbles in the device. Nevertheless, various challenges have been highlighted during this thesis. It was predictable that the effect of electrode geometry and electrode size configuration within a photoelectrochemical reactor would affect the performance of the device, and further adjustments are needed to improve this first prototype. The first two research questions that drove this project could not be answered in a quantitative manner: Measuring the scaled-up cell without contacts, in an open becker confirmed the working principles are scalable. However, the complete device performance and activity could not be properly evaluated and/or compared to the literature. This lack of perspective is due to the impossibility of obtaining the hydrogen yield at the current setup.

As for the stability of the cell, it was not possible to evaluate it since the time interval of the experiment was far below the assumed one. As the theoretical calculations suggested, the hypothesized time was approximately 72 hours, with light-on intervals of 8 hours, in our case, the experiment was carried out for less than 15 minutes due to the emptying of the glass separators and the fact that no gas was able to reach the cylinders in the water tank.

A proper answer can be given to the final research question. By only increasing the size of the cell, leaving the same configuration for both the catalyst and the electrolyte is not enough to reach the industrial step. It is true that in the work of Zhu *et al.*, there were no membranes to separate the produced gasses and that there was no pumping system, which eventually added some losses in the setup. But it is also true that some extra precautions are needed to create a fully functioning reactor. While striving for the optimal balance between functionality and production efficiency, further research and innovation are necessary to develop a device that can cut the "Gordian knot" of simultaneously achieving ultra-high stability (>10,000 h) and high efficiency (>15%).

Bibliography

[1] Hannah Ritchie, Max Roser, and Pablo Rosado. "Energy". In: *Our World in Data* (2022). https://ourworldindata.org/energy.

[2] Nathan S. Lewis and Daniel G. Nocera. "Powering the Planet: Chemical Challenges in Solar Energy Utilization". In: *Proceedings of the National Academy of Sciences of the United States of America* 103.43 (Oct. 24, 2006), pp. 15729–15735. ISSN: 0027-8424. DOI: 10.1073/pnas.0603395103. pmid: 17043226.

[3] Oscar Khaselev and John A. Turner. "A Monolithic Photovoltaic-Photoelectrochemical Device for Hydrogen Production via Water Splitting". In: *Science* 280.5362 (Apr. 17, 1998), pp. 425–427. DOI: 10.1126/science.280.5362.425. URL: https://www.science.org/doi/10.1126/science.280.5362.425 (visited on 05/15/2023).

[4] Xinwei Sun et al. "Earth-Abundant Electrocatalysts in Proton Exchange Membrane Electrolyzer". In: (2018). DOI: 10.20944/preprints201811.0077.v2. URL: https://doi.org/10.20944/preprints201811.0077.v2 (visited on 05/15/2023).

[5] Junjie Zhu et al. "Double Perovskite Cobaltites Integrated in a Monolithic and Noble Metal-Free Photoelectrochemical Device for Efficient Water Splitting". In: *ACS applied materials & interfaces* 13.17 (May 5, 2021), pp. 20313–20325. ISSN: 1944-8252. DOI: 10.1021/acsami.1c01900. pmid: 33904298.

[6] Erik Verlage et al. "A Monolithically Integrated, Intrinsically Safe, 10% Efficient, Solar-Driven Water-Splitting System Based on Active, Stable Earth-Abundant Electrocatalysts in Conjunction with Tandem III–V Light Absorbers Protected by Amorphous TiO2 Films". In: *Energy & Environmental Science* 8.11 (Oct. 28, 2015), pp. 3166–3172. ISSN: 1754-5706. DOI: 10.1039/C5EE01786F. URL: https://pubs.rsc.org/en/content/articlelanding/2015/ee/c5ee01786f (visited on 05/15/2023).

[7] Fuel Cells and Hydrogen 2 Joint Undertaking (EU body or agency) Now known as et al. *Study on Hydrogen from Renewable Resources in the EU: Final Report*. LU: Publications Office of the European Union, 2016. ISBN: 978-92-9246-139-3. URL: https://data.europa.eu/doi/10.2843/28276 (visited on 05/15/2023).

[8] Akira Fujishima and Kenichi Honda. “Electrochemical Photolysis of Water at a Semiconductor Electrode”. In: *Nature* 238.5358 (5358 July 1972), pp. 37–38. ISSN: 1476-4687. DOI: 10.1038/238037a0. URL: https://www.nature.com/articles/238037a0 (visited on 05/15/2023).

[9] Roel Van De Krol and Michael Grätzel, eds. *Photoelectrochemical Hydrogen Production*. Vol. 102. Electronic Materials: Science & Technology. Boston, MA: Springer US, 2012. ISBN: 978-1-4614-1379-0 978-1-4614-1380-6. DOI: 10.1007/978-1-4614-1380-6. URL: https://link.springer.com/10.1007/978-1-4614-1380-6 (visited on 05/15/2023).

[10] P Hersch, K Zweibel, and Solar Energy Research Institute. “Basic Photovoltaic Principles and Methods”. In: (). DOI: 10.2172/5191389.

[11] D. E. Carlson and C. R. Wronski. “Amorphous Silicon Solar Cells”. In: *Amorphous Semiconductors*. Ed. by Marc H. Brodsky. Topics in Applied Physics. Berlin, Heidelberg: Springer, 1985, pp. 287–329. ISBN: 978-3-540-70751-6. DOI: 10.1007/3-540-16008-6_164. URL: https://doi.org/10.1007/3-540-16008-6_164 (visited on 09/24/2023).

[12] Tao Cheng et al. “Explanation of Dramatic pH-Dependence of Hydrogen Binding on Noble Metal Electrode: Greatly Weakened Water Adsorption at High pH”. In: *Journal of the American Chemical Society* 140.25 (June 27, 2018), pp. 7787–7790. ISSN: 0002-7863. DOI: 10.1021/jacs.8b04006. URL: https://doi.org/10.1021/jacs.8b04006 (visited on 09/24/2023).

[13] Nasir Mahmood et al. “Electrocatalysts for Hydrogen Evolution in Alkaline Electrolytes: Mechanisms, Challenges, and Prospective Solutions”. In: *Advanced Science* 5.2 (2018), p. 1700464. ISSN: 2198-3844. DOI: 10.1002/advs.201700464. URL: https://onlinelibrary.wiley.com/doi/abs/10.1002/advs.201700464 (visited on 09/24/2023).

[14] Shan Wang, Aolin Lu, and Chuan-Jian Zhong. “Hydrogen Production from Water Electrolysis: Role of Catalysts”. In: *Nano Convergence* 8.1 (Feb. 11, 2021), p. 4. ISSN: 2196-5404. DOI: 10.1186/s40580-021-00254-x. URL: https://doi.org/10.1186/s40580-021-00254-x (visited on 09/24/2023).

[15] Charles C. L. McCrory et al. “Benchmarking Hydrogen Evolving Reaction and Oxygen Evolving Reaction Electrocatalysts for Solar Water Splitting Devices”. In: *Journal of the American Chemical Society* 137.13 (Apr. 8, 2015), pp. 4347–4357. ISSN: 1520-5126. DOI: 10.1021/ja510442p. pmid: 25668483.

[16] Fabio Dionigi et al. “In-Situ Structure and Catalytic Mechanism of NiFe and CoFe Layered Double Hydroxides during Oxygen Evolution”. In: *Nature communications* 11.1 (May 1, 2020), p. 2522. ISSN: 2041-1723. DOI: 10.1038/s41467-020-16237-1.

pmid: 32433529. URL: https://europepmc.org/articles/PMC7239861 (visited on 08/10/2023).

[17] Fang Song et al. "Transition Metal Oxides as Electrocatalysts for the Oxygen Evolution Reaction in Alkaline Solutions: An Application-Inspired Renaissance". In: *Journal of the American Chemical Society* 140.25 (June 27, 2018), pp. 7748–7759. ISSN: 1520-5126. DOI: 10.1021/jacs.8b04546. pmid: 29788720.

[18] Mingquan Yu, Eko Budiyanto, and Harun Tüysüz. "Principles of Water Electrolysis and Recent Progress in Cobalt-, Nickel-, and Iron-Based Oxides for the Oxygen Evolution Reaction". In: *Angewandte Chemie International Edition* 61.1 (2022), e202103824. ISSN: 1521-3773. DOI: 10.1002/anie.202103824. URL: https://onlinelibrary.wiley.com/doi/abs/10.1002/anie.202103824 (visited on 08/10/2023).

[19] J. Tyler Mefford et al. "Water Electrolysis on La1xSrxCoO3 Perovskite Electrocatalysts". In: *Nature Communications* 7.1 (1 Mar. 23, 2016), p. 11053. ISSN: 2041-1723. DOI: 10.1038/ncomms11053. URL: https://www.nature.com/articles/ncomms11053 (visited on 09/24/2023).

[20] Kevin J. May et al. "Influence of Oxygen Evolution during Water Oxidation on the Surface of Perovskite Oxide Catalysts". In: *The Journal of Physical Chemistry Letters* 3.22 (Nov. 15, 2012), pp. 3264–3270. DOI: 10.1021/jz301414z. URL: https://doi.org/10.1021/jz301414z (visited on 09/24/2023).

[21] Sophia Haussener et al. "Modeling, Simulation, and Design Criteria for Photoelectrochemical Water-Splitting Systems". In: *Energy & Environmental Science* 5.12 (Nov. 14, 2012), pp. 9922–9935. ISSN: 1754-5706. DOI: 10.1039/C2EE23187E. URL: https://pubs.rsc.org/en/content/articlelanding/2012/ee/c2ee23187e (visited on 05/31/2023).

[22] J. Reichman. "The Current-voltage Characteristics of Semiconductor-electrolyte Junction Photovoltaic Cells". In: *Applied Physics Letters* 36.7 (July 23, 2008), pp. 574–577. ISSN: 0003-6951. DOI: 10.1063/1.91551. URL: https://doi.org/10.1063/1.91551 (visited on 05/15/2023).

[23] Krishnan Rajeshwar, Robert McConnell, and Stuart Licht, eds. *Solar Hydrogen Generation*. New York, NY: Springer, 2008. ISBN: 978-0-387-72809-4 978-0-387-72810-0. DOI: 10.1007/978-0-387-72810-0. URL: http://link.springer.com/10.1007/978-0-387-72810-0 (visited on 05/15/2023).

[24] Yuliang Sun et al. "Chapter 14 - Applications of MXenes and Their Composites in Catalysis and Photoelectrocatalysis". In: *Mxenes and Their Composites*. Ed. by Kishor Kumar Sadasivuni et al. Micro and Nano Technologies. Elsevier, Jan. 1, 2022, pp. 449–498. ISBN: 978-0-12-823361-0. DOI: 10.1016/B978-0-12-823361-0.00007-1. URL: https://www.sciencedirect.com/science/article/pii/B9780128233610000071 (visited on 05/15/2023).

[25] Akihiko Kudo and Yugo Miseki. "Heterogeneous Photocatalyst Materials for Water Splitting". In: *Chemical Society Reviews* 38.1 (Dec. 16, 2008), pp. 253–278. ISSN: 1460-4744. DOI: 10.1039/B800489G. URL: https://pubs.rsc.org/en/content/articlelanding/2009/cs/b800489g (visited on 05/15/2023).

[26] Peter Ritterskamp et al. "A Titanium Disilicide Derived Semiconducting Catalyst for Water Splitting under Solar Radiation—Reversible Storage of Oxygen and Hydrogen". In: *Angewandte Chemie International Edition* 46.41 (2007), pp. 7770–7774. ISSN: 1521-3773. DOI: 10.1002/anie.200701626. URL: https://onlinelibrary.wiley.com/doi/abs/10.1002/anie.200701626 (visited on 05/15/2023).

[27] *Visible-Light Photocatalysis in Nitrogen-Doped Titanium Oxides | Science*. URL: https://www.science.org/doi/10.1126/science.1061051 (visited on 05/15/2023).

[28] Peter Y. Yu and Manuel Cardona. *Fundamentals of Semiconductors: Physics and Materials Properties*. Graduate Texts in Physics. Berlin, Heidelberg: Springer, 2010. ISBN: 978-3-642-00709-5 978-3-642-00710-1. DOI: 10.1007/978-3-642-00710-1. URL: https://link.springer.com/10.1007/978-3-642-00710-1 (visited on 05/15/2023).

[29] H. Gerischer. "Solar Photoelectrolysis with Semiconductor Electrodes". In: *Solar Energy Conversion: Solid-State Physics Aspects*. Ed. by Bernhard O. Seraphin. Topics in Applied Physics. Berlin, Heidelberg: Springer, 1979, pp. 115–172. ISBN: 978-3-540-35369-0. DOI: 10.1007/3-540-09224-2_4. URL: https://doi.org/10.1007/3-540-09224-2_4 (visited on 05/15/2023).

[30] Eric L. Miller. "Solar Hydrogen Production by Photoelectrochemical Water Splitting: The Promise and Challenge". In: *On Solar Hydrogen & Nanotechnology*. John Wiley & Sons, Ltd, 2010, pp. 1–35. ISBN: 978-0-470-82399-6. DOI: 10.1002/9780470823996.ch1. URL: https://onlinelibrary.wiley.com/doi/abs/10.1002/9780470823996.ch1 (visited on 05/15/2023).

[31] C. N. Kenyon et al. "Behavior of Si Photoelectrodes under High Level Injection Conditions. 3. Transient and Steady-State Measurements of the Quasi-Fermi Levels at Si/CH3OH Contacts". In: *The Journal of Physical Chemistry B* 101.15 (Apr. 1, 1997), pp. 2850–2860. ISSN: 1520-6106. DOI: 10.1021/jp962485c. URL: https://doi.org/10.1021/jp962485c (visited on 05/15/2023).

[32] Eric L. Miller et al. "Optimization of Hybrid Photoelectrodes for Solar Water-Splitting". In: *Electrochemical and Solid-State Letters* 8.5 (Mar. 24, 2005), A247. ISSN: 1944-8775. DOI: 10.1149/1.1887196. URL: https://iopscience.iop.org/article/10.1149/1.1887196/meta (visited on 05/15/2023).

[33] Richard E. Rocheleau and Eric L. Miller. “Photoelectrochemical Production of Hydrogen: Engineering Loss Analysis”. In: *International Journal of Hydrogen Energy* 22.8 (Aug. 1, 1997), pp. 771–782. ISSN: 0360-3199. DOI: 10.1016/S0360-3199(96)00221-2. URL: https://www.sciencedirect.com/science/article/pii/S0360319996002212 (visited on 05/15/2023).

[34] Masafumi Yamaguchi, Tatsuya Takamoto, and Kenji Araki. “Super High-Efficiency Multi-Junction and Concentrator Solar Cells”. In: *Solar Energy Materials and Solar Cells*. 14th International Photovoltaic Science and Engineering Conference 90.18 (Nov. 23, 2006), pp. 3068–3077. ISSN: 0927-0248. DOI: 10.1016/j.solmat.2006.06.028. URL: https://www.sciencedirect.com/science/article/pii/S0927024806002194 (visited on 05/15/2023).

[35] D. F. Swinehart. “The Beer-Lambert Law”. In: *Journal of Chemical Education* 39.7 (July 1962), p. 333. ISSN: 0021-9584, 1938-1328. DOI: 10.1021/ed039p333. URL: https://pubs.acs.org/doi/abs/10.1021/ed039p333 (visited on 05/15/2023).

[36] Greg P. Smestad. “Optoelectronics of Solar Cells”. In: SPIE, July 3, 2002. ISBN: 978-0-8194-8049-1. DOI: 10.1117/3.446028. URL: https://spiedigitallibrary.org/ebooks/PM/Optoelectronics-of-Solar-Cells/eISBN-9780819480491/10.1117/3.446028 (visited on 05/15/2023).

[37] Bruce Parkinson. “On the Efficiency and Stability of Photoelectrochemical Devices”. In: *Accounts of Chemical Research* 17.12 (Dec. 1, 1984), pp. 431–437. ISSN: 0001-4842, 1520-4898. DOI: 10.1021/ar00108a004. URL: https://pubs.acs.org/doi/abs/10.1021/ar00108a004 (visited on 05/15/2023).

[38] Arthur B. Ellis et al. “Study of N-Type Semiconducting Cadmium Chalcogenide-Based Photoelectrochemical Cells Employing Polychalcogenide Electrolytes”. In: *Journal of the American Chemical Society* 99.9 (Apr. 1977), pp. 2839–2848. ISSN: 0002-7863, 1520-5126. DOI: 10.1021/ja00451a001. URL: https://pubs.acs.org/doi/abs/10.1021/ja00451a001 (visited on 05/15/2023).

[39] Michael G. Walter et al. “Solar Water Splitting Cells”. In: *Chemical Reviews* 110.11 (2010). PMID: 21062097, pp. 6446–6473. DOI: 10.1021/cr1002326. eprint: https://doi.org/10.1021/cr1002326. URL: https://doi.org/10.1021/cr1002326.

[40] Mark S. Wrighton, Peter T. Wolczanski, and Arthur B. Ellis. “Photoelectrolysis of Water by Irradiation of Platinized N-Type Semiconducting Metal Oxides”. In: *Journal of Solid State Chemistry* 22.1 (Sept. 1, 1977), pp. 17–29. ISSN: 0022-4596. DOI: 10.1016/0022-4596(77)90185-2. URL: https://www.sciencedirect.com/science/article/pii/0022459677901852 (visited on 05/19/2023).

[41] Arthur J. Nozik and Rüdiger Memming. "Physical Chemistry of SemiconductorLiquid Interfaces". In: *The Journal of Physical Chemistry* 100.31 (Jan. 1, 1996), pp. 13061–13078. ISSN: 0022-3654. DOI: 10.1021/jp953720e. URL: https://doi.org/10.1021/jp953720e (visited on 05/19/2023).

[42] Nicholas C. Strandwitz et al. "Photoelectrochemical Behavior of N-Type Si(100) Electrodes Coated with Thin Films of Manganese Oxide Grown by Atomic Layer Deposition". In: *The Journal of Physical Chemistry C* 117.10 (Mar. 14, 2013), pp. 4931–4936. ISSN: 1932-7447, 1932-7455. DOI: 10.1021/jp311207x. URL: https://pubs.acs.org/doi/10.1021/jp311207x (visited on 05/19/2023).

[43] A. E. Delahoy et al. "A One-Unit Photovoltaic Electrolysis System Based on a Triple Stack of Amorphous Silicon (Pin) Cells". In: *International Journal of Hydrogen Energy* 10.2 (Jan. 1, 1985), pp. 113–116. ISSN: 0360-3199. DOI: 10.1016/0360-3199(85)90043-6. URL: https://www.sciencedirect.com/science/article/pii/0360319985900436 (visited on 05/19/2023).

[44] G. H. Lin et al. "One Step Method to Produce Hydrogen by a Triple Stack Amorphous Silicon Solar Cell". In: *Applied Physics Letters* 55.4 (July 24, 1989), pp. 386–387. ISSN: 0003-6951, 1077-3118. DOI: 10.1063/1.101879. URL: https://pubs.aip.org/aip/apl/article/55/4/386-387/56386 (visited on 05/19/2023).

[45] James R. Bolton, Stewart J. Strickler, and John S. Connolly. "Limiting and Realizable Efficiencies of Solar Photolysis of Water". In: *Nature* 316.6028 (6028 Aug. 1985), pp. 495–500. ISSN: 1476-4687. DOI: 10.1038/316495a0. URL: https://www.nature.com/articles/316495a0 (visited on 05/19/2023).

[46] Michael G. Walter et al. "Solar Water Splitting Cells". In: *Chemical Reviews* 110.11 (Nov. 10, 2010), pp. 6446–6473. ISSN: 0009-2665. DOI: 10.1021/cr1002326. URL: https://doi.org/10.1021/cr1002326 (visited on 05/15/2023).

[47] J.-P. Becker et al. "A Modular Device for Large Area Integrated Photoelectrochemical Water-Splitting as a Versatile Tool to Evaluate Photoabsorbers and Catalysts". In: *Journal of Materials Chemistry A* 5.10 (Mar. 7, 2017), pp. 4818–4826. ISSN: 2050-7496. DOI: 10.1039/C6TA10688A. URL: https://pubs.rsc.org/en/content/articlelanding/2017/ta/c6ta10688a (visited on 05/22/2023).

[48] Kristine Tolod, Simelys Hernández, and Nunzio Russo. "Recent Advances in the BiVO4 Photocatalyst for Sun-Driven Water Oxidation: Top-Performing Photoanodes and Scale-Up Challenges". In: *Catalysts* 7.12 (Jan. 1, 2017), p. 13. ISSN: 2073-4344. DOI: 10.3390/catal7010013. URL: http://www.mdpi.com/2073-4344/7/1/13 (visited on 05/22/2023).

[49] Haijiao Lu et al. “Single-Source Bismuth (Transition Metal) Polyoxovanadate Precursors for the Scalable Synthesis of Doped BiVO4 Photoanodes”. In: *Advanced Materials (Deerfield Beach, Fla.)* 30.46 (Nov. 2018), e1804033. ISSN: 1521-4095. DOI: 10.1002/adma.201804033. pmid: 30285284.

[50] Wilson A. Smith. “Photoelectrochemical Cell Design, Efficiency, Definitions, Standards, and Protocols”. In: *Photoelectrochemical Solar Fuel Production: From Basic Principles to Advanced Devices*. Ed. by Sixto Giménez and Juan Bisquert. Cham: Springer International Publishing, 2016, pp. 163–197. ISBN: 978-3-319-29641-8. DOI: 10.1007/978-3-319-29641-8_4. URL: https://doi.org/10.1007/978-3-319-29641-8_4 (visited on 05/22/2023).

[51] Alexis Grimaud et al. “Double Perovskites as a Family of Highly Active Catalysts for Oxygen Evolution in Alkaline Solution”. In: *Nature Communications* 4.1 (1 Sept. 17, 2013), p. 2439. ISSN: 2041-1723. DOI: 10.1038/ncomms3439. URL: https://www.nature.com/articles/ncomms3439 (visited on 06/07/2023).

[52] In: (). URL: https://hayata.com/wp-content/uploads/catalog-stainless-steel-chemical-resistance-charts.pdf.

[53] Nian-Tzu Suen et al. “Electrocatalysis for the Oxygen Evolution Reaction: Recent Development and Future Perspectives”. In: *Chemical Society Reviews* 46.2 (Jan. 23, 2017), pp. 337–365. ISSN: 1460-4744. DOI: 10.1039/C6CS00328A. URL: https://pubs.rsc.org/en/content/articlelanding/2017/cs/c6cs00328a (visited on 07/14/2023).

[54] R. Kötz et al. “Oxygen Evolution on Ru and Ir Electrodes: XPS-studies”. In: *Journal of Electroanalytical Chemistry and Interfacial Electrochemistry*. Electronic and Molecular Structure of Electrode-Electrolyte Interface 150.1 (July 25, 1983), pp. 209–216. ISSN: 0022-0728. DOI: 10.1016/S0022-0728(83)80203-4. URL: https://www.sciencedirect.com/science/article/pii/S0022072883802034 (visited on 07/14/2023).

[55] R. Kötz, H. Neff, and S. Stucki. “Anodic Iridium Oxide Films: XPS-Studies of Oxidation State Changes And”. In: *Journal of The Electrochemical Society* 131.1 (Jan. 1, 1984), p. 72. ISSN: 1945-7111. DOI: 10.1149/1.2115548. URL: https://iopscience.iop.org/article/10.1149/1.2115548/meta (visited on 07/14/2023).

[56] M. M. Jakšić. “Advances in Electrocatalysis for Hydrogen Evolution in the Light of the Brewer-Engel Valence-Bond Theory”. In: *International Journal of Hydrogen Energy* 12.11 (Jan. 1, 1987), pp. 727–752. ISSN: 0360-3199. DOI: 10.1016/0360-3199(87)90090-5. URL: https://www.sciencedirect.com/science/article/pii/0360319987900905 (visited on 09/30/2023).

[57] Chonglun Fan et al. “Study of Electrodeposited Nickel-Molybdenum, Nickel-Tungsten, Cobalt-Molybdenum, and Cobalt-Tungsten as Hydrogen Electrodes in Alkaline Water Electrolysis”. In: *Journal of The Electrochemical Society* 141.2 (Feb. 1, 1994), p. 382. ISSN: 1945-7111. DOI: 10.1149/1.2054736. URL: https://iopscience.iop.org/article/10.1149/1.2054736/meta (visited on 07/10/2023).

[58] Einar Vøllestad et al. “Mixed Proton and Electron Conducting Double Perovskite Anodes for Stable and Efficient Tubular Proton Ceramic Electrolysers”. In: *Nature Materials* 18.7 (7 July 2019), pp. 752–759. ISSN: 1476-4660. DOI: 10.1038/s41563-019-0388-2. URL: https://www.nature.com/articles/s41563-019-0388-2 (visited on 07/12/2023).

[59] Håkon Andersen et al. “A Highly Efficient Electrocatalyst Based on Double Perovskite Cobaltites with Immense Intrinsic Catalytic Activity for Water Oxidation”. In: *Chemical Communications* 56.7 (Jan. 23, 2020), pp. 1030–1033. ISSN: 1364-548X. DOI: 10.1039/C9CC08765F. URL: https://pubs.rsc.org/en/content/articlelanding/2020/cc/c9cc08765f (visited on 07/12/2023).

[60] Lei Han, Shaojun Dong, and Erkang Wang. “Transition-Metal (Co, Ni, and Fe)-Based Electrocatalysts for the Water Oxidation Reaction”. In: *Advanced Materials* 28.42 (2016), pp. 9266–9291. ISSN: 1521-4095. DOI: 10.1002/adma.201602270. URL: https://onlinelibrary.wiley.com/doi/abs/10.1002/adma.201602270 (visited on 07/12/2023).

[61] Ram Subbaraman et al. “Trends in Activity for the Water Electrolyser Reactions on 3d M(Ni,Co,Fe,Mn) Hydr(Oxy)Oxide Catalysts”. In: *Nature Materials* 11.6 (6 June 2012), pp. 550–557. ISSN: 1476-4660. DOI: 10.1038/nmat3313. URL: https://www.nature.com/articles/nmat3313 (visited on 07/12/2023).

[62] Nancy Li et al. “Detection of High-Valent Iron Species in Alloyed Oxidic Cobaltates for Catalysing the Oxygen Evolution Reaction”. In: *Nature Communications* 12.1 (1 July 9, 2021), p. 4218. ISSN: 2041-1723. DOI: 10.1038/s41467-021-24453-6. URL: https://www.nature.com/articles/s41467-021-24453-6 (visited on 07/12/2023).

[63] Jin Suntivich et al. “A Perovskite Oxide Optimized for Oxygen Evolution Catalysis from Molecular Orbital Principles”. In: *Science* 334.6061 (Dec. 9, 2011), pp. 1383–1385. DOI: 10.1126/science.1212858. URL: https://www.science.org/doi/10.1126/science.1212858 (visited on 07/12/2023).